



Performance evaluation of nanofluid-enhanced biomimetic liquid-cooled heat sinks for efficient thermal management applications

Hamza Babar^{a,*}, Hongwei Wu^{a,*}, Mahmoud Eltaweel^a, Wenbin Zhang^b

^a School of Physics, Engineering and Computer Science, University of Hertfordshire, Hatfield AL10 9AB, United Kingdom

^b School of Science and Technology, Nottingham Trent University, Clifton Lane, Nottingham NG11 8NS, United Kingdom

ARTICLE INFO

Keywords:

Thermal management
Nanofluid
Liquid cooling
Heat sink
Heat transfer

ABSTRACT

Efficient thermal management is critical in high-power-density systems found in electronics, electric vehicles, renewable energy devices, aerospace platforms, and data centres. This study aims to enhance thermal performance through the development of nature-inspired heat sink geometries integrated with advanced nanofluids. Two novel biomimetic configurations, Inline Arranged Airfoil Integrated Curvilinear Pin-Fin (IACPF) and Inline Arranged Airfoil Integrated Corrugated Curvilinear Pin-Fin (AICCPF) were experimentally evaluated across heating powers of 75–300 W and flow rates ranging from 200 to 450 mL/min. These heat sinks were tested using mono and hybrid nanofluids formulated with silver (Ag), silicon carbide (SiC), and beryllium oxide (BeO) nanoparticles, chosen for their high thermal conductivity, dispersion stability, and economic viability. The experimental methodology focused on assessing thermal and hydraulic performance through key parameters including Nusselt number, thermal resistance, wall temperature, and pressure drop. Comparative study showed that, using water as the working fluid at 75 W, the AICCPF heat sink delivered a 10.23% improvement in Nusselt number over the IACPF. When benchmarked against a conventional straight-channel heat sink, the AICCPF design at 150 W demonstrated a 103% enhancement in Nusselt number, confirming its geometric effectiveness. Among nanofluids, the highest convective enhancement was achieved using Ag/SiC hybrid nanofluid, yielding a peak improvement of 22.29% in the AICCPF configuration. Pressure drops remained within manageable limits, with a maximum increase of 15.86%. These findings demonstrate that combining biomimetic heat sink architectures with thermally optimised nanofluids achieves high thermal performance while maintaining acceptable hydraulic penalties. The proposed approach offers scalable, energy-efficient solutions for next-generation cooling applications.

1. Introduction

Liquid cooling has become increasingly vital in modern electronics cooling, particularly as artificial intelligence (AI) and high-performance computing (HPC) workloads push the boundaries of thermal management and energy efficiency. Conventional air cooling, once sufficient for traditional processors, now struggles with thermal bottlenecks, making it an unsustainable choice for densely packed systems or devices with high heat flux densities. Liquid cooling offers superior thermal conductivity, enabling more effective heat dissipation and allowing for denser configurations without compromising performance.

According to the Data Centre Frontier Liquid Cooling Technology Transition Report, a staggering 93% of organizations are now adopting direct-to-chip liquid cooling in some capacity, from early pilots to full-

scale deployments, with only 7% reporting no adoption plans [1]. This trend underscores the industry's recognition of liquid cooling as a critical component in meeting the demands of modern computing environments. Further emphasizing this shift, the Uptime Institute's 2023 Cooling Systems Survey indicates that direct liquid cooling is expected to surpass air cooling as the primary method for IT infrastructure cooling by the end of the decade [2]. Companies like Supermicro, Google, and Hewlett Packard Enterprise are leading the way by integrating liquid cooling solutions into their systems, highlighting the technology's growing importance in the industry.

The ongoing miniaturisation and increased functional density of electronic and power systems have led to a substantial rise in heat flux levels. This thermal intensification accelerates material degradation, compromises long-term reliability, and imposes significant limitations on device performance, energy efficiency, and operational safety. While

* Corresponding authors.

E-mail addresses: h.babar@herts.ac.uk (H. Babar), h.wu6@herts.ac.uk (H. Wu).

<https://doi.org/10.1016/j.ijheatmasstransfer.2025.127498>

Received 19 April 2025; Received in revised form 20 June 2025; Accepted 30 June 2025

Available online 7 July 2025

0017-9310/© 2025 The Authors. Published by Elsevier Ltd. This is an open access article under the CC BY license (<http://creativecommons.org/licenses/by/4.0/>).

Nomenclature*List of abbreviations*

Ag	silver
AI	artificial intelligence
AICCPF	inline arranged airfoil integrated corrugated curvilinear Pin-Fin
BeO	beryllium oxide
Fe ₂ O ₃	ferric oxide
HPC	high-performance computing
IACPF	inline arranged airfoil integrated curvilinear Pin-Fin
MCHS	microchannel heat sink
SDBS	sodium dodecylbenzene sulfonate
SiC	silicon carbide
TDP	thermal design power
TiO ₂	titania
XRD	X-ray diffraction

List of symbols

$A_{fin,top}$	top surface area of the fin (m^2)
A_{seff}	effective convection area (m^2)
A_{avg}	average cross-sectional area (m^2)
A_w	wall surface area (m^2)
C_p	specific heat capacity of the fluid (J/kg·K)
d_h	hydraulic diameter (m)
f	darcy friction factor
H	height (m)

k_c	thermal conductivity of coolant (W/m·K)
k_s	thermal conductivity of solid (heat sink) material (W/m·K)
L	length (m)
$L_{a,fin}$	active length of airfoil fin (m)
L_s, W_s	length and width of heat sink base (m)
\dot{m}	mass flow rate (kg/s)
μ	dynamic viscosity (Pa·s)
ρ	fluid density (kg/m ³)
Nu	Nusselt number
P_f	effective fin perimeter (m)
PP	pumping power (W)
q	volumetric flow rate (m ³ /s)
\dot{Q}	heat transfer rate (m ³ /s)
Re	Reynolds number
R_{th}	thermal resistance (K/W)
S_{sec}	wetted perimeter/side surface area of flow section (m^2)
T_{inlet}	fluid inlet temperature (°C or K)
T_{outlet}	fluid outlet temperature (°C or K)
T_{mean}	mean bulk temperature of the fluid (°C or K)
T_w	wall temperature (°C or K)
T_b	base temperature of the heat sink (°C or K)
v	average fluid velocity (m/s)
V_{sec}	volume of flow section (m ³)
ΔP	pressure drop (Pa)
l_x	distance from base to channel wall (m)
$LMTD$	log mean temperature difference (°C or K)

liquid cooling has emerged as a viable approach to manage such heat loads, its effectiveness is fundamentally governed by the thermal properties of the working fluid. Therefore, enhancing coolant performance is critical to achieving high-efficiency thermal management in modern high-power-density applications. Conventional coolants like water and ethylene glycol, while widely used, often fail to provide sufficient heat dissipation in modern, high-density systems, prompting the need for more effective alternatives [3]. Their limited thermal conductivity and inability to efficiently transfer heat in high-density systems have prompted the search for alternative solutions. To address these shortcomings, research is increasingly focused on the development of advanced working fluids like nanofluids suspensions of nanoparticles in base fluids.

Nanofluids have demonstrated improved convective heat transfer characteristics, thermal conductivity, and surface wettability in comparison to traditional fluids. The enhancement mechanisms, primarily attributed to Brownian motion, thermophoresis, and particle-fluid interactions, are further intensified in hybrid nanofluids, which incorporate two or more types of nanoparticles [4]. Hybrid suspensions are of particular interest due to their ability to exploit the distinct advantages of different nanoparticles, potentially offering a more stable and thermally efficient medium for heat dissipation. These fluids in combination with efficient heat sinks are now being considered not only in processors cooling but also in sectors such as electric vehicles (EVs), renewable energy, and space technologies [5–7]. For instance, McKinsey estimates that electric vehicles will constitute over 30% of global vehicle sales by 2030, significantly amplifying the demand for efficient thermal management solutions in battery and power electronics systems. Abood et al. [8] numerically investigated mixed convection of a water-based Ag–MgO hybrid nanofluid within a magnetised square cavity. Their findings revealed that substituting water with the hybrid nanofluid enhanced convective flow, particularly at higher Reynolds and Richardson numbers, and significantly improved thermal energy transport, resulting in a marked increase in the average Nusselt number. Ellahi et al. [9] investigated the potential of kerosene–Al₂O₃ nanofluid to

enhance regenerative cooling in the thrust chambers of semi-cryogenic rocket engines, emphasising its superior thermal performance over conventional coolants. Their results revealed that dispersing alumina nanoparticles in kerosene substantially improves heat transfer characteristics, positioning the nanofluid as a viable and efficient coolant for high-heat-flux applications.

In parallel with the development of advanced coolants, there has been considerable progress in the design of micro-scale heat exchangers. Among these, microchannel heat sinks (MCHSs) and mini-channel configurations embedded with pin-fin structures have received widespread attention [10–12]. These geometries not only increase the heat transfer surface area but also promote secondary flows and local turbulence, thereby improving the thermal performance of the system. However, the enhancement in heat transfer is often accompanied by a substantial increase in pressure drop, leading to higher pumping power requirements. This trade-off between thermal enhancement and hydraulic performance necessitates the careful optimisation of channel and fin geometries, as well as coolant selection.

Consequently, researchers have turned towards hybrid thermal management solutions that combine geometrical optimization with tailored nanofluids. This integrated approach aims to achieve significant improvements in heat transfer while maintaining acceptable pressure drop levels. In particular, bio-inspired designs, mimicking structures found in nature, are gaining traction for their efficiency and adaptability. The fish gill structure, for instance, presents an elegant example of low-resistance, high-efficiency fluid exchange that has evolved to support respiration in aquatic environments. Such analogies offer valuable insights into the development of compact and high-performance heat sinks.

Li et al. [13] proposed a novel single-phase microchannel heat sink featuring a pyramid thermal dissipation unit embedded with nature-inspired channel designs to effectively manage ultra-high heat fluxes. Using a 3D conjugate heat transfer model, they demonstrated that the pyramid structure could degrade extreme heat flux from 10³ to 10² W/cm², while maintaining chip temperatures below 120 °C. Their

findings revealed that the integration of spiral cooling tubes with bionic microchannel patterns not only enhanced temperature uniformity and heat transfer but also allowed for a significant reduction in the minimum required thermal conductivity of materials, broadening material selection options and simplifying system complexity compared to existing high-flux cooling technologies. Acharya [14] conducted a comprehensive numerical study on the thermo-fluidic behaviour of a microchannel heat sink (MCHS) with various fin configurations, designed to dissipate a heat flux of 50 W/cm^2 typical for high-power electronic devices. The research investigated three fin shapes: square fins, 45° oriented square fins, and elliptical fins, arranged in both inline and staggered configurations. The number of fins varied from 11×3 to 79×3 (fins per row \times rows), with heights ranging from $100 \mu\text{m}$ to $300 \mu\text{m}$. To isolate the shape effect on heat transfer and frictional loss, the researchers maintained constant cross-sectional area and surface area for all fin types. Numerical simulations were performed using ANSYS Fluent, employing a Finite Volume Method based multigrid solver, considering laminar flow conditions with Reynolds numbers ranging from 100 to 400. The findings revealed that heater surface temperature decreased monotonously with the increasing number of fins for heights above $200 \mu\text{m}$, with elliptical fins showing marginally better heat transfer. Additionally, it was also observed that staggered configurations outperformed inline arrangements in terms of heat transfer and elliptical fins in a staggered arrangement showed the least frictional resistance. Mehboob et al. [15] carried out a comprehensive numerical study to optimise bioconvective heat transfer in magnetohydrodynamic (MHD) Eyring–Powell nanofluids infused with motile microorganisms, considering the effects of variable viscosity and porous media in ciliated microchannels. Their results demonstrated that increasing the viscosity parameter leads to a reduction in nanofluid temperature.

Wang et al. [16] proposed a novel butterfly-shaped channel structure for liquid cooling of prismatic battery modules. They compared the cooling performance of their design with traditional designs, including serpentine, straight, and leaf-shaped channels, considering factors like maximum temperature, temperature difference, and pressure drop. The butterfly-shaped channel demonstrated optimal overall performance based on desirability function calculations. After optimizing structural parameters, they achieved a 29.1% decrease in maximum temperature compared to the other configuration. The authors also investigated the effect of mass flow on thermal performance, finding that increased coolant mass flow rate led to decreased maximum temperature and temperature difference, though the rate of descent gradually slowed. At a mass flow rate of 5 g/s , the maximum temperature was 30.86°C with a 4.96°C temperature difference. It was concluded that some complex bionic structures, while effective at cooling, can increase energy consumption due to higher pressure losses. The butterfly-shaped design emerged to strike a balance between enhanced cooling performance and manageable pressure drop.

Alkhazaleh et al. [17] explored the thermal and hydraulic performance of microelectromechanical systems (MEMS) heat sinks incorporating straight microchannels and square pin-fins, specifically designed for liquid cooling in microelectronic devices. Their work focused on understanding the effects of geometric design on thermal performance and pumping power. The study concluded that the inclusion of square pin fins reduced thermal resistance significantly, achieving up to a 51% decrease at higher Reynolds numbers. However, this improvement came at the cost of increased pumping power, attributed to enhanced boundary layer disturbances and the generation of secondary flows. The results also showed that enlarging the hydraulic diameter of the microchannel reduced both the pumping power and thermal resistance. Pazarlıoğlu et al. [18] conducted a detailed numerical investigation to enhance convective heat transfer and fluid dynamics in sudden expansion tubes (SETs) by integrating capsule-type dimpled fins (CTDFs) and hybrid nanofluids composed of Ag and MgO nanoparticles. The study analysed various expansion angles (30° – 90°) and nanofluid formulations under laminar flow conditions, focusing on energy, exergy, and

entropy generation. The results demonstrated that a 45° expansion angle combined with 0.5% Ag–1.5% MgO hybrid nanofluid and CTDFs offered the optimal configuration, improving average Nusselt number by 20%, reducing entropy generation by 23%, and enhancing exergy output by 26%. Despite a moderate increase in pressure drop and second law losses due to higher pumping power, the findings highlight the effectiveness of combining geometric and fluid enhancements to achieve superior thermal performance, providing valuable insights for advanced heat exchanger and cooling system designs.

The configuration and layout of pin fins are critical factors affecting a heat sink's performance, particularly in terms of heat transfer enhancement and pressure drop behaviour. Parameters such as the spacing, height, orientation, and distribution of the fins influence the system's ability to optimise heat dissipation while limiting flow resistance. Well-optimised pin-fin arrangements can boost turbulence and improve the heat transfer coefficient, thereby enhancing thermal dissipation. However, such gains often result in higher pressure drops due to increased resistance to flow. Therefore, achieving a balance between thermal efficiency and acceptable pressure losses is vital, especially in compact and high-performance cooling systems. Duangthongsuk et al. [19] analysed how diamond-shaped pin-fin configurations impact the heat transfer and flow characteristics of nanofluid-cooled heat sinks. The researchers compared inline and staggered arrangements using copper heat sinks with dimensions of $33 \text{ mm} \times 30 \text{ mm}$. Tests were performed with de-ionized (DI) water and SiO_2 -water nanofluids across various particle volume concentrations and Reynolds numbers from 100 to 600 under laminar flow conditions. Results indicated that both increased Reynolds numbers and higher nanoparticle concentrations enhanced thermal performance. Notably, the staggered configuration outperformed the inline design by 3–10% in terms of heat transfer. Furthermore, the use of nanofluids did not significantly affect pressure drop or pumping power. The authors developed predictive correlations for the Nusselt number and pressure drop, with most results aligning within $\pm 10\%$ of the experimental data. Gao et al. [20] analysed the pressure drop characteristics of microchannel heat sinks with various pin-fin arrangement patterns. Results revealed that partially uniform/gradient stagger pin-fin arrangements demonstrated higher pressure drops due to increased flow obstruction and narrower gaps between the fins and channel sidewalls. Additionally, they observed that pressure drop decreased with increasing heat flux due to the reduction in fluid viscosity and density as the fluid temperature rose. Gijoy et al. [21] performed a 3D numerical simulation to investigate the heat transfer characteristics of elliptical-cylindrical asymmetric pin fin heat sink (ECAPFHS) under turbulent flow, aiming to optimise its structure. The study revealed notable improvements in heat transfer efficiency with the ECAPFHS design. According to the results, in the first phase of their research, the highest fin effectiveness for solid ECAPFs was 1.43, achieved at a fin radius to channel height ratio of 0.9. However, further enhancements were observed by introducing perforations, with fins featuring 8 holes of 3 mm diameter reaching a maximum fin effectiveness of 2.25 at a Reynolds number of 3111. The perforated heat sink not only boosted thermal performance but also reduced fin volume by up to 60% compared to the reference cylindrical pin fin heat sink. The findings highlighted the potential of employing strategic techniques, which could be highly valuable in improving thermal performance while balancing other factors such as material usage and design complexity. Hamza and Ali [22] the thermal and hydraulic performance of aerofoil-shaped pin-fin heat sink using titania (TiO_2) and ferric oxide (Fe_2O_3) nanofluids, comparing the results with distilled water as the base fluid. The research focused on varying heating power and Reynolds number to analyse the heat transfer characteristics. Their findings revealed significant enhancements in heat transfer performance, with the average Nusselt number increasing by 14.5% for TiO_2 -water and 15.89% for Fe_2O_3 -water nanofluids at 0.01 vol% concentration and 25 W heating power. However, these improvements came with increased pumping power requirements, with Fe_2O_3 nanofluid showing a 42.46% increase

and TiO₂ nanofluid a 30.5% increase. The aerofoil shape was chosen for its superior fluid dynamics and heat transfer properties, offering delayed flow separation, enhanced heat transfer, reduced pressure drop, and optimised flow characteristics. The researchers emphasise the importance of using hybrid cooling techniques, such as mini-channel heat sinks combined with nanofluids, to address the challenges of heat dissipation in miniaturised devices. A study conducted by Pazarlıoğlu [23] numerically investigated the thermodynamic performance of heatsinks featuring different pin fin geometries (circular, square, and hexagonal) filled with a ferro-nanofluid composed of Fe₃O₄ nanoparticles suspended in water with a volumetric concentration of 2%. Under laminar flow conditions, the study evaluated key parameters such as convective heat transfer, pressure drop, figure of merit, and entropy generation. Their findings indicated that the square pin fin configuration yielded the highest thermal performance, with an 18.41% increase in average Nusselt number and a 7.71% reduction in total entropy generation at $Re = 2000$ compared to the base case using water. However, the square fins also showed a significant enhancement in pressure drop, with an increase of nearly 59%.

Bahiraei et al. [24] carried out a two-phase numerical study analysing silver-water nanofluid flow within an elliptical pin-fin heat sink to enhance thermal management in electronic systems. The study examined various nanoparticle volume fractions, fin densities, and Reynolds numbers using a mixture-based two-phase model and the four-equation transition Shear Stress Transport (SST) model for turbulent flow. It was found that introducing nanoparticles to the base fluid significantly promoted uniform temperature distribution, reduced surface temperature and thermal resistance, and improved the heat transfer coefficient. Augmenting the volume fraction by 0.4% at a fin density of 0.168 and Reynolds number of 2500 led to a 16.2% reduction in thermal resistance and a 25.5% enhancement in heat transfer coefficient. Additionally, increasing fin density from 0.036 to 0.168 resulted in a 49.6% improvement in heat transfer coefficient. The study also noted that pumping power and figure of merit increased with higher volume fractions and fin densities. Ellahi [25] conducted an analytical investigation into the MHD flow of non-Newtonian nanofluids through a pipe, considering temperature-dependent viscosity effects. Using homotopy analysis method (HAM), they derived explicit expressions for velocity, temperature, and nanoparticle concentration. It was observed that increasing the thermophoresis parameter reduced the thermal and flow profiles, while enhancing Brownian motion led to improved thermal transport. The findings highlight the importance of nanofluid properties in optimising convective heat transfer under complex flow conditions. Han et al. [26] performed an integrated design and optimisation of a liquid-cooled heat sink for a 30 kW motor inverter in electric vehicles, addressing the challenges posed by high-power-density electronic systems. Their study compared three heat sink configurations: counter-flow, double U-shaped, and serpentine channels and the results of temperature distribution and fluid velocity fields revealed that the serpentine channel configuration provided superior temperature uniformity and cooling characteristics. The research also investigated how variations in geometric parameters (such as fin thickness) and flow rates affected overall thermal performance, leading to an optimised configuration. It is concluded that the serpentine configuration's superior performance can be attributed to its ability to provide better fluid mixing and heat transfer due to its winding path. A key aspect of this research is the emphasis on integrated design in heat sink development. By arranging cooling channels directly beneath power devices, the team ensured temperature uniformity and targeted cooling. This approach not only enhances cooling efficiency but also reduces pump power requirements compared to conventional designs.

A substantial number of studies have investigated nanofluid-enhanced heat sinks, exploring a wide range of configurations such as microchannels, pin-fin arrays, slotted and grooved surfaces, and biomimetic geometries [27,28]. These works have demonstrated varying degrees of heat transfer improvement, often dependent on nanoparticle

type, concentration, flow regime, and the geometrical characteristics of the heat sink. While significant progress has been made in optimising individual parameters such as nanofluid composition, fin geometry, or flow conditions, there remains limited integration of biomimetic design principles with advanced coolant strategies. To better position the present study within this research landscape, Table 1 summarises key contributions from recent literature, detailing the types of nanofluids employed, particle concentrations, heat sink geometries, materials, and performance outcomes.

This study presents a comprehensive investigation into two novel biomimetic heat sink configurations, IACPF and AICCPF, which draw inspiration from the fluidic architecture of aquatic respiration systems. These designs are engineered to replicate the efficient flow pathways observed in fish, where fluid passes both around and through internal structures to maximise exchange efficiency with minimal resistance. The central aim of this work is to evaluate the thermal and hydraulic performance of these geometries under varying operational and fluidic conditions, thereby assessing their suitability for next-generation thermal management in high heat-flux applications such as electronics cooling, power electronics, and compact energy systems.

Unlike conventional pin-fin arrays or straight-channel heat sinks, the proposed configurations feature a hybrid fin structure that promotes both internal and external fluid interaction, effectively enhancing convective heat transfer while maintaining manageable pressure losses. To the best of the authors' knowledge, these specific configurations and their integrated design philosophy have not been previously explored in the literature, establishing a novel paradigm in the development of high-performance, compact thermal management solutions.

To further augment the heat dissipation capability of these geometries, carefully selected mono and hybrid nanofluids were employed as working fluids. The nanofluids were formulated using Ag, SiC, and BeO nanoparticles, including binary hybrid combinations such as Ag/SiC, Ag/BeO, and SiC/BeO. These materials were chosen based on their complementary attributes: Ag for its exceptionally high thermal conductivity, SiC for its chemical and thermal stability, and BeO for its cost-effectiveness and favourable thermophysical behaviour compared to other oxides like titania, alumina, etc. By integrating these advanced thermal coolants with biomimetic heat sink architectures, this study introduces an integrated thermal management strategy that synergistically combines geometric innovation with optimised coolant characteristics to enhance overall cooling performance.

Moving forward, the design configurations proposed in this study could be adapted for thermal management in systems where efficient removal of excess heat is essential [29–32]. In electric vehicles (EVs), such geometries could be beneficial for enhancing the cooling of battery packs and power electronics, particularly under high thermal loads during fast charging or extended operation. Beyond traditional cooling applications, the design philosophy demonstrated here holds promise for novel engineering challenges. For instance, compact and efficient cooling structures could be embedded in drones, flying cars, and urban air mobility (UAM) platforms to manage the thermal loads of propulsion systems, battery units, and navigation electronics. In wearable and biomedical devices, miniaturised adaptations of these configurations may provide a pathway to control unwanted heat without adding bulk or noise. Although these applications are beyond the scope of the current experimental validation, the demonstrated performance benefits of the proposed heat sink designs offer a promising foundation for further development and integration into emerging cooling technologies.

2. Heat sink design configurations, manufacturing, and features

An optimised heat sink design is characterised by its ability to maximise the heat transfer area and enhance interaction with the working fluid while maintaining minimal flow resistance. After an extensive review of current literature and recent advancements in heat sink technologies, it has been observed that most studies primarily focus

Table 1
Summary of some recent literature on nanofluid-enhanced heat sinks, highlighting nanoparticle types, concentrations, heat sink configurations, base materials, experimental objectives, and key performance outcomes.

References	Working Fluid		Heat Sink Configuration			Objectives	Results (Key Points)
	Particles-Basefluid	Particle concentration (φ)	Fins or channel shape	Material	Dimensional parameters		
Duangthongsuk et al. [19]	Silica (SiO ₂) -water	Particle volume fractions tested were 0.2%, 0.4%, and 0.6%.	Diamond-shaped micro-pin-fin. Inline and staggered layouts.	Copper	- 30 mm x 33 mm dimensions - 1.0 mm hydraulic diameter	Examine the effects of pin-fin layout, Re , and φ on cooling performance, performance index (PI), and pressure drop (ΔP).	- Thermal performance augmented with increasing Re and φ . - Staggered layout had 3–10% higher thermal performance than inline. - Small effect on ΔP and pumping power. - New correlations for Nusselt number and ΔP proposed.
Ghadikolaei et al. [33]	Functionalized Graphene Nanoplatelets (CGNPs) -water	0.025% wt, 0.050% wt, 0.075%wt, and 0.100%wt	Sneaky fins with nature-inspired baseplate designs (honeycomb, ternate veiny, snowflake, spider netted)	Copper, Nickel, and Silver	40 mm x 40 mm	To investigate the combined effect of nature-inspired geometries and eco-friendly nanofluids on thermal performance and fluid flow for CPU cooling.	- Spider netted baseplate reduced maximum liquid block temperature by 8.5 K compared to ternate veiny design. - Optimal thermal output improvement (8.5% vs. simple model) achieved with spider netted baseplate and 0.075%wt nanofluid. - Copper heat sink outperformed nickel in cooling efficiency due to superior thermal properties.
Shahsavari et al. [34]	Silver (Ag) -water	$\varphi = 0 - 1\%$	The heat sink configuration explored in the study features Tesla valve-based helical channels.	Copper	- 11.48 mm length, 9.60 mm width, 0.4 mm height. - 0.2 mm thick cover. - Circular inlet (0.7 mm diameter) and four circular outlets (0.4 mm diameter each)	- Investigate hydrothermal performance of nanofluid-cooled heat sink. - Analyse entropy generation in Tesla valve-based microchannels.	- Improved CPU cooling and lowered thermal resistance with a higher Reynolds number. - Heat sink with Tesla valve-based helical channels outperforms plain channels. - Pumping power increased with higher Re . - Peak Performance Evaluation Criterion was 1.642 for $Re = 500$ and $\varphi = 0\%$
Kong et al. [35]	De-Ionised water	-	Microchannels fabricated on silicon wafers.	Silicon wafers Coated with Copper inverse opals	Channel Dimensions: Width = 50, 100, 200 μm ; Height = 100 μm . - Coating (6–8 μm thickness, 5 μm pore size). - Manifold: PDMS 3D structure, 900 μm height.	- Achieve extreme cooling for electronics with high heat flux (>1 kW/cm ²). - Optimise microchannel and manifold designs for efficient thermal and hydraulic performance.	- Heat flux removal up to 1147 W/cm ² with a convective thermal resistance of 0.068 cm ² ·K/W and total pressure drop of 32 kPa. - Enhanced thermal uniformity (<6 K deviation). - Promotes nucleate boiling at higher heat fluxes.
Zhang et al. [36]	Water	-	Bionic limulus-like fins (BLLF) inspired by the horseshoe crab (Limulus)	Aluminium	- Length: 140 mm, Width: 65 mm, Thickness of cooling plate: 3 mm, Microchannel thickness: 2 mm, Splitter length: 120 mm, Splitter width: 6.876 mm - Horizontal distance between fins: 3.437 mm	- Improve the cooling efficiency and reduce pressure loss in channel-type liquid cooling plates for battery thermal management systems (BTMS) in electric vehicles. - Optimise fin geometry and arrangement (spacing ratios) for best thermal and hydraulic performance.	- Best performance (lowest average temperature and pressure drop) achieved when the fin size and spacing were equal in both directions. - Proposed BLLF outperformed conventional rectangular and oval fins in both average temperature and pressure drop.

(continued on next page)

Table 1 (continued)

References	Working Fluid		Heat Sink Configuration			Objectives	Results (Key Points)
	Particles-Basefluid	Particle concentration (φ)	Fins or channel shape	Material	Dimensional parameters		
Gupta and Subbarao [37]	Alumina (Al ₂ O ₃)-water	The concentration of the nanofluid varied from 1% to 4% (w/w).	Parallel arrays of channel or tunnel-like structures	–	–	<ul style="list-style-type: none"> - Assess cooling efficacy, heat transfer coefficient, thermohydraulic performance, and loss in concentration of alumina nanofluids in MCHS - Investigate the impact of nanofluids on back axial conduction at low Reynolds numbers ($10 \leq Re \leq 50$) - Develop correlations to predict Nusselt number and friction factor for MCHS based on nanofluid concentration - Explain the increase in heat transfer coefficient considering thermophoresis and Brownian motion of nanoparticles. 	<ul style="list-style-type: none"> - 51.54% reduction in back axial conduction compared to base fluid. - Up to 29% lower surface temperatures in the microchannel heat sink. - Enhancement in heat transfer coefficient up to 43.34%. - Nusselt number increased up to 35.85% at Reynolds number 50. - Optimal thermohydraulic performance of 1.17 at 3% (w/w) nanoparticle concentration and Reynolds number 50.
Ma et al. [38]	Ag (Silver), SiO ₂ (Silica), Al ₂ O ₃ (Alumina), Water as Base Fluid	Volume Fraction: 0–6%	Three shapes: <ul style="list-style-type: none"> - Rectangular (MC-R) - Trapezoidal (MC-T) - Omega-shaped (MC-O) 	Silicon	<ul style="list-style-type: none"> - 0.4 mm width, 0.3 mm height, 10 mm length - Hydraulic Diameter: 0.2 mm 	<ul style="list-style-type: none"> - Investigate the thermal-hydraulic performance of nanofluids. - Optimise microchannel design. - Compare performance with and without nanoparticles. - Analyse the impact of different cross-sectional geometries. - Assess entropy generation and energy efficiency. 	<ul style="list-style-type: none"> - Al₂O₃ nanofluids increased HTC by 12.3% at $Re = 500$. - MC-O showed the highest HTC and lowest max temperature. - SiO₂ exhibited the lowest performance improvement. - Best COP observed with Ag in MC-R. - Total entropy generation reduced in MC-O. - Best cooling performance at 0.3% (rectangular grooves) and 0.4% (cylindrical bulges). - Surface temperature reduction: up to 12.4% for grooves, 11.7% for bulges compared to water. - Higher Reynolds numbers improve heat transfer but may reduce exergy efficiency due to increased pressure drops.
Zhao et al. [39]	TiO ₂ -water	0.0% – 0.5% wt%	Rectangular grooves and cylindrical bulges Arrangements: Aligned, Staggered	Copper	Depth: 1 mm, 2 mm; Width: 2 mm; Material: Copper; Dimensions: 50 mm x 50 mm (external).	<ul style="list-style-type: none"> - Investigate the thermo-hydraulic performance of nanofluids in enhanced CPU heat sinks. - Explore exergy efficiency as a function of nanofluid concentration and Reynolds number. - Assess comprehensive evaluation indices for different configurations and conditions. 	<ul style="list-style-type: none"> - Best cooling performance at 0.4% (cylindrical bulges). - Surface temperature reduction: up to 12.4% for grooves, 11.7% for bulges compared to water. - Higher Reynolds numbers improve heat transfer but may reduce exergy efficiency due to increased pressure drops.
Sun et al. [40]	Silicon carbide (SiC)-water	$\varphi = 0.01, 0.03, \text{ and } 0.1 \text{ vol\%}$	Matrix rib micro-jet	Copper	<ul style="list-style-type: none"> - 6 x 6 matrix rib design - Channel (30 mm x 30 mm), Fin (3 mm x 3 mm x 1 mm) 	<ul style="list-style-type: none"> - Optimise cooling performance for concentrated solar cells. - Combine impinging jet and microchannel for enhanced cooling. - Evaluate influence of nanofluid concentration on heat sink performance. 	<ul style="list-style-type: none"> - 6.5% increase in convective heat transfer coefficient compared to water. - 2.8% reduction in cooling surface temperature. - Improved temperature uniformity.
Wang et al. [41]	Water	–	Plate fin (baseline), Petaloid I (circular pins), Petaloid II (pit pins), Pinwheel-like, Honeycombed	Copper	<ul style="list-style-type: none"> - Heat sink external dimensions: 200 mm x 100 mm x 7 mm - Flow channel area with fins: 160 mm (length) x 90 mm (width) - Fin/channel height: 1.5 mm - Inlet/outlet pipe inner diameter: 6 mm 	Experimentally investigate the thermal-hydraulic performance of four novel pin-fin heat sink geometries (petaloid I & II, pinwheel-like, and honeycombed) compared to a conventional plate-fin heat sink	<ul style="list-style-type: none"> - Honeycombed PFHS showed the highest heat transfer coefficient (21.5 kW/m²·K) and lowest friction factor among all designs. - Petaloid I achieved the highest Nusselt number due to its smaller hydraulic diameter.

(continued on next page)

Table 1 (continued)

References	Working Fluid		Heat Sink Configuration			Objectives	Results (Key Points)
	Particles-Basefluid	Particle concentration (ϕ)	Fins or channel shape	Material	Dimensional parameters		
Qi et al. [42]	Al ₂ O ₃ -water TiO ₂ -water	0.1–2.0 wt% 0.1–1.0 wt%	Plate	Copper	Plate Size: 50 mm × 50 mm Plate Thickness: 2 mm Inlet/Outlet Diameter: 5 mm	<ul style="list-style-type: none"> - Investigate thermo-hydraulic performance of nanofluids in CPU cooling. - Study effects of nanoparticle mass fraction on heat transfer. 	<ul style="list-style-type: none"> - Al₂O₃-water - Reduced CPU temperature by 23.2% compared to water. - Best thermal performance at a critical concentration of 1.0%. - TiO₂-water - Reduced CPU temperature by 14.9% compared to water. - Best thermal performance was noted at a concentration of 0.4%.
Yusof et al. [43]	Boron nitride nanotubes (BNN)-water	0.001% – 0.03% by weight	Rectangular micro-channel heat sink	–	Dimensions: Length=1 cm, Width=1 cm, Height=533 μ m, Channel Height=320 μ m, Wall Thickness=213 μ m	<ul style="list-style-type: none"> - Minimize thermal resistance and pressure drop. - Investigate optimal coolant concentration. - Explore efficient microchannel geometries using a heuristic approach. 	<ul style="list-style-type: none"> - Reduction in thermal resistance by 5.34% at 0.01% concentration compared to water. - Lowest thermal resistance achieved: 0.0711 K/W at 0.01% concentration. - Pumping power increased with channel narrowing and higher fluid viscosity.
Baig et al. [44]	Al ₂ O ₃ -water, TiO ₂ -water	0.005 vol%, 0.01 vol%	Dual flow slotted fin mini-channel heat sink	Copper	Slot thickness: 0.5 mm Angle: 45° Fin Spacing: 0.5 mm	Investigate heat transfer enhancement using nanofluids in slotted fin configurations	<ul style="list-style-type: none"> - Reduction in base temperature up to 15.28%. - Heat transfer increased by 4.35%. - TiO₂-Water increases heat transfer but is less efficient than Al₂O₃-Water. - Minor pressure drop increase noted.
Ghasemi et al. [45]	Al ₂ O ₃ -water	–	Circular structure of mini-channel heat sink	Aluminium	Three different heat sinks with varying hydraulic diameters (4, 6, 8 mm) Fabrication: Wire-cutting technique	<ul style="list-style-type: none"> - Optimise heat sink geometry for enhanced CPU cooling. - Investigate trade-offs between heat transfer and pressure drop. - Evaluate heat sink performance under various flow rates. 	<ul style="list-style-type: none"> - Reduced hydraulic diameter improves heat transfer. - Increased flow rate enhances heat transfer. - Nanofluid increases convective heat transfer but at the cost of higher pressure drop.

on heat transfer performance as the defining criterion for efficiency. However, factors like pressure drop, an equally critical parameter, are often not given due consideration. For an efficient thermal management system, balancing heat transfer performance with flow resistance is essential to ensure the system's overall effectiveness.

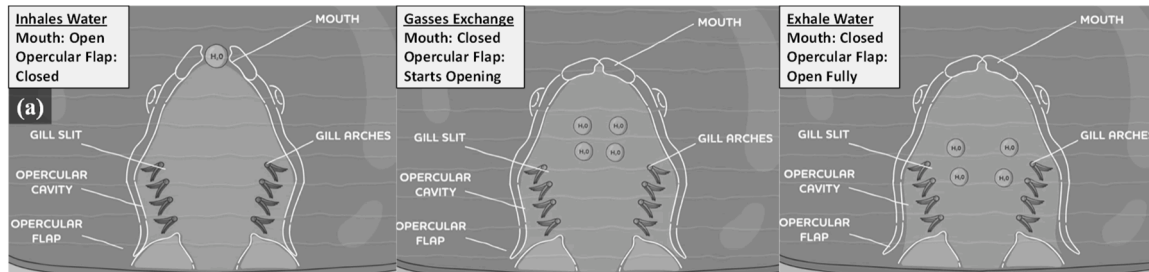
2.1. Fins design inspiration

The present study introduces innovative heat sink designs inspired by the respiratory system of fish. Fish utilise an exceptional mechanism for fluid movement, where water flows not only around their bodies but also inside-out through their gills, enabling effective oxygen exchange with minimal resistance. A study conducted by Stevens on gas exchange in tuna revealed that the average rate of water flow over the gills was 2.8 L/min per kilogram of body weight [46]. The perfection of nature is evident in the design of fish, where their external body and the inside-out flow of water through the mouth for respiration assist in smooth movement with minimal resistance. Drawing inspiration from these principles, novel hybrid pin-fin heat sink geometries have been designed and manufactured. These hybrid pin-fins are a combination of

two distinct shapes, designed to allow water to flow both over and through a confined passage. The internal pin-fins, shaped like an airfoil, replace the fish's internal organs, while the external structure consists of curvilinear or corrugated curvilinear pin-fins inspired by the body shapes of tuna and the black ghost knifefish (BGKF). The unique fins shape ensures improved heat transfer by increasing the effective surface area while maintaining low pressure drop characteristics.

In this biomimetic design, an exit passage analogous to the opercular valve is strategically positioned at the trailing edges, rather than on either side just behind the mouth as it is in fish, as illustrated in Fig. 1. This adjustment aligns with the engineering requirements of the heat sink design while retaining the inspiration from natural fluid dynamics. The proposed configurations are named Inline Arranged Airfoil Integrated Curvilinear Pin-Fin Heat Sink (IACPF) and Inline Arranged Airfoil Integrated Corrugated Curvilinear Pin-Fin Heat Sink (AICCPF). As this design evolves through further investigation, it holds the potential to be adapted for a variety of applications in the marine, automotive, and aerospace industries. To the best of the authors' knowledge, such hybrid configurations have not been explored from this perspective before. This study is expected to attract the attention of researchers and encourage

**Design Inspiration
Fish Respiratory System**



Schematic representation of the fish respiratory system illustrating the sequential flow of water during inhalation, gas exchange, and exhalation phases—serving as the biological inspiration for the heat sink design.

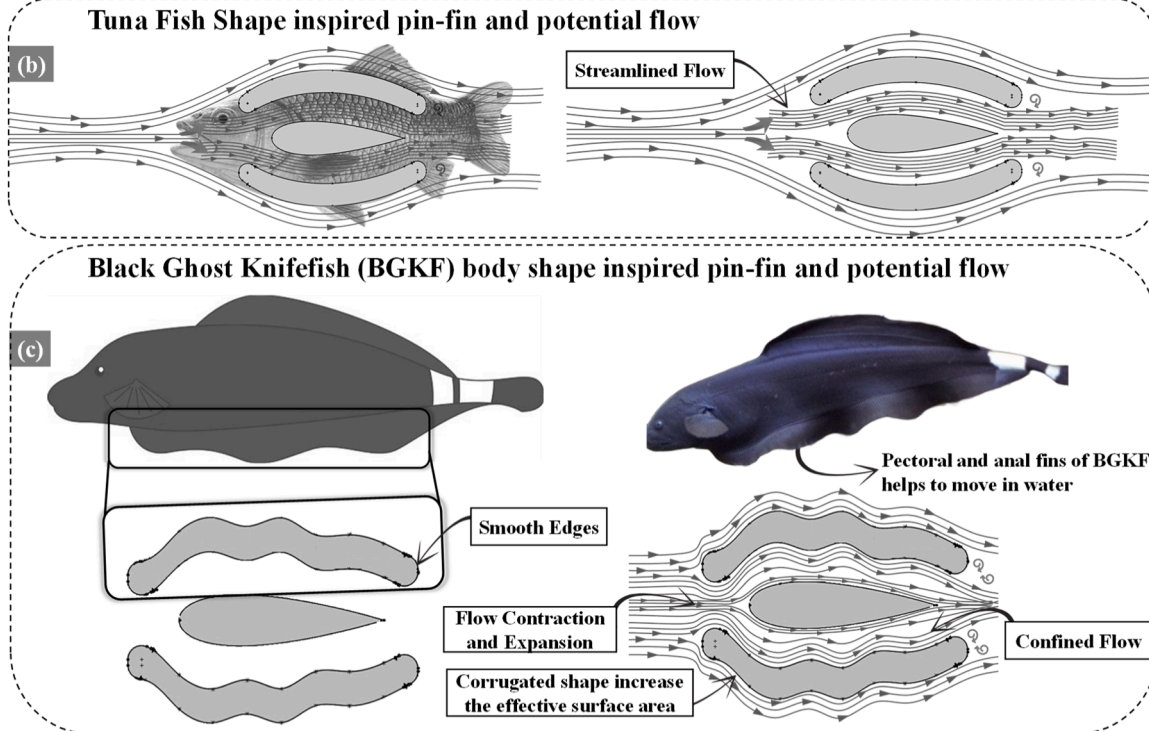


Fig. 1. (a) Schematic representation of the fish respiratory system, Conceptual design sketches of hybrid pin-fin geometries inspired by fish morphology, (b) Tuna fish-shaped curvilinear fins for streamlined flow and low resistance, (c) Corrugated fins inspired by the pectoral and anal fins of the Black Ghost Knifefish (BGKF) for enhanced surface area and heat transfer performance.

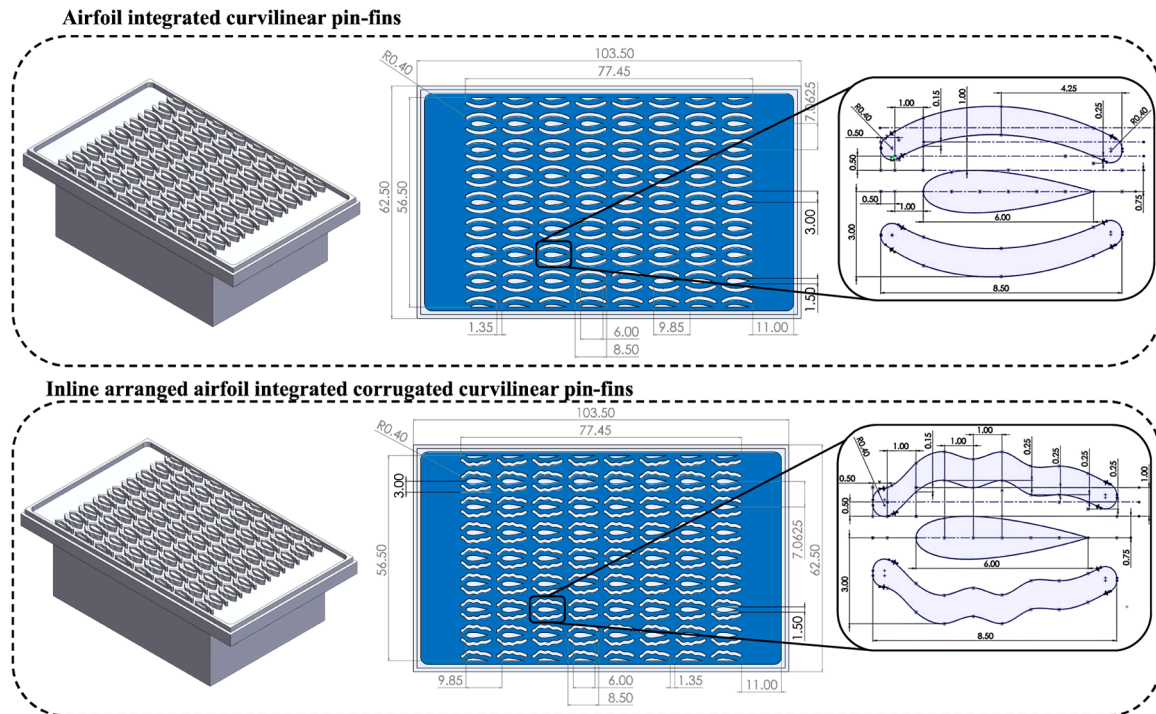


Fig. 2. Dimensional specifications and fin arrangement of the (a) In-line Arranged Airfoil Integrated Curvilinear Pin-Fin Heat Sink (IACPF), highlighting the integration of airfoil-shaped inner fins with outer curvilinear pin-fins, (b) In-line Arranged Airfoil Integrated Corrugated Curvilinear Pin-Fin Heat Sink (AICCPF), showing the integration of airfoil inner fins and outer corrugated curvilinear fins inspired by BGKF morphology.

further exploration of these designs for various applications.

The first configuration features an inline arrangement of airfoil integrated curvilinear pin fins. The curvilinear geometry depicts the body shape of the tuna fish, known for its streamlined form that minimises resistance during movement in water. Fig. 2(a) provides a detailed representation of the fins and their dimensional specifications. In the second configuration, AICCPF, the curvilinear pin fins are replaced with corrugated curvilinear pin fins. These fins draw inspiration from the pectoral and anal fins of the BGKF, a species that lacks caudal fins and generates propulsion using its pectoral and anal fins to move in water. The corrugated shape not only offers a more effective surface area for heat transfer but also causes little disruption to fluid flow which ultimately improves the cooling capacity. The detailed dimensions and arrangement of the fins are illustrated in Fig. 2(b).

For the airfoil geometry, the symmetrical NACA 0025 profile has been adopted. This design features a chord length of 6 mm and a fixed width of 1.5 mm. The airfoil-shaped fins are bordered by curvilinear and corrugated curvilinear pin fins, forming hybrid pin-fin configurations. These hybrid designs combine fins of varying shapes to synergistically enhance performance, ensuring both efficient thermal management and minimal flow resistance.

2.2. Dimensional considerations and materials selection

The dimensions of the finned section have been carefully determined to align with the size specifications of Intel® Xeon® processors, including the silver, gold, and platinum series. These processors are widely recognised for their high-performance capabilities in applications such as multimedia processing, graphics rendering, engineering simulations, and large-scale transactional database servers. Additionally, they are integral to supporting Internet infrastructure and high-volume computational tasks. A 10 mm space has been allocated for the inlet and outlet plenum on each side. A comprehensive study was conducted to analyse the thermal behaviour of Intel® Xeon® processors, which generate heat ranging from 50 W to 300 W under varying

workloads. This range underscores the critical need for efficient thermal management solutions. Fig. 3 provides a graphical illustration of the base temperatures and thermal design power (TDP) values for various Xeon® processor models. These values indicate the safe case temperature thresholds corresponding to specific TDP levels. Exceeding these temperature limits can result in a significant decline in processor performance, and in extreme cases, may lead to irreversible damage or burning of the processor.

The pin-fins on the heat sink surface are designed with a balance between manufacturability and thermal performance. To ensure practical fabrication, the channel width is set to accommodate machining tools of 1 mm or smaller, preventing excessive manufacturing complexity and costs. While narrower channels could enhance heat transfer, they would also lead to a significant increase in pressure drop and machining cost. The height of the pin-fins is maintained at 2 mm, allowing for effective thermal contact while ensuring compatibility with confined spaces.

Aluminium stands out as the material of choice for heat sink fabrication due to its exceptional combination of properties. Its impressive thermal conductivity ensures efficient heat dissipation, while its lightweight nature makes it a practical option for applications where reducing overall weight is crucial. Compared to alternatives like copper and silver, aluminium is not only more affordable but also offers superior corrosion resistance, enhancing its durability in diverse environments. Furthermore, its ease of manufacturing allows for intricate designs, and its recyclability supports sustainable practices, making aluminium an ideal candidate for electronic and industrial applications demanding reliable thermal management solutions.

In this study, the heat sink dimensions have been tailored specifically for Xeon® processors. However, the versatile design of these heat sinks ensures their applicability across a wide range of devices and application areas. The proposed designs are engineered to not only meet the current thermal management requirements of Xeon® processors but also accommodate the demands of future, more advanced processors with higher TDP values. This adaptability positions these heat sinks as

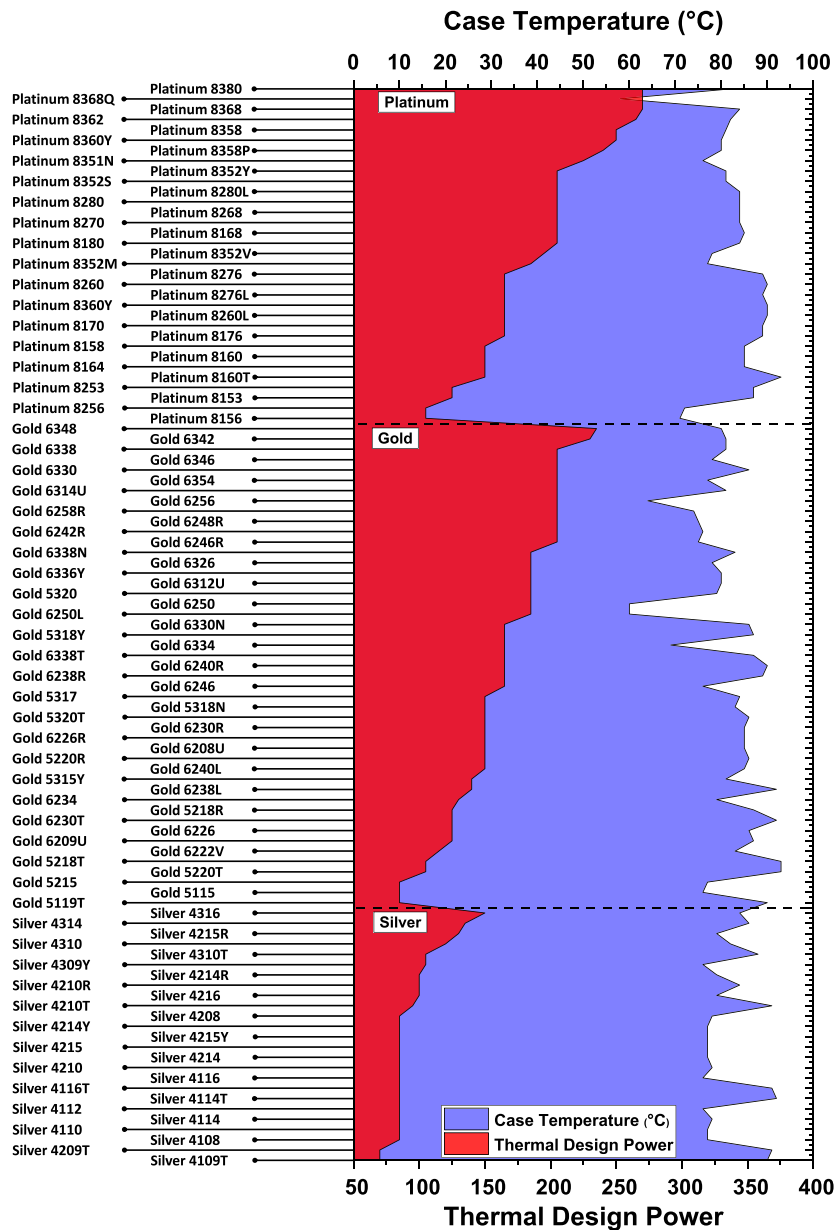


Fig. 3. Comparison of base temperatures and thermal design power (TDP) ratings for various Intel® Xeon® processor models, illustrating the thermal management demands associated with each class.

reliable solutions for both present and next-generation high-performance computing systems.

2.3. Manufacturing

The heat sinks were fabricated using 3-axis CNC milling, chosen due to its widespread accessibility and precision capabilities, which made it an ideal method for producing intricate geometries while maintaining cost-effectiveness. The design was tailored to accommodate a 0.7 mm diameter tool for grooving all the channels, ensuring an efficient and streamlined manufacturing process, as evidenced in Fig. 4. Precision was a critical focus, with a tolerance of 0.05 mm being readily achievable. However, reducing the tolerance to 0.01 mm proved both technically challenging and cost-prohibitive. To optimise performance and manufacturability, the design emphasised key dimensions such as fin spacing and hole size over excessively tight tolerances. Key considerations in the design and manufacturing process include:

Tool Selection: A smaller 0.7 mm tool was used to address the size

complexity, ensuring precision in channel grooving while maintaining structural integrity. Additionally, the design accommodated practical tooling and machining strategies to balance precision with cost and time constraints.

Impact of Reduced Spacing: Narrower channel spacings, such as 0.5 mm, significantly increase both processing time and cost. Maintaining precision in such cases required additional steps to avoid damaging adjacent fin walls, complicating production.

Tolerance Management: A practical tolerance of 0.05 mm was adopted to ensure manufacturability without incurring exponential cost increases.

Feasibility Limitations: Spacings as tight as 0.1 mm exceeded the capability of standard equipment, making machining impractical and misaligned with agile manufacturing principles due to the steep rise in costs and time demands.

Ultimately, the design struck a balance between manufacturability, cost-efficiency, and performance by focusing on achievable tolerances and practical geometries.

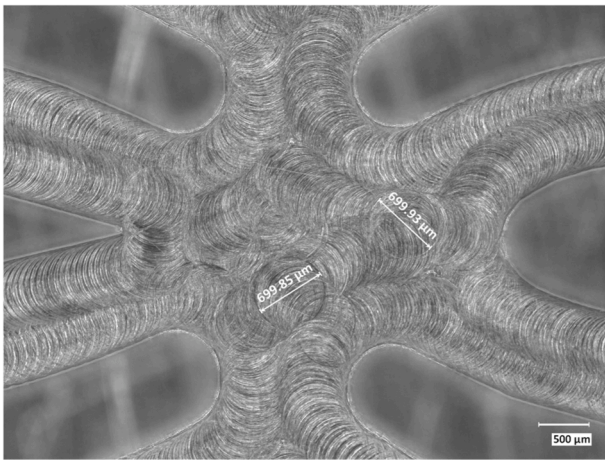


Fig. 4. CNC-machined heat sink, showcasing the precision grooving and structural symmetry achieved using a 0.7 mm diameter tool.

2.4. Surface morphology

The surface morphology of the fabricated heat sinks was examined using scanning electron microscopy (SEM) to analyse the texture and machining-induced features. The SEM images, as shown in Fig. 5, reveal distinct surface patterns characterised by tool movement during the milling process. These patterns result in micro-impressions that contribute to the overall surface roughness, which can influence thermal performance by promoting micro-turbulence in the working fluid. However, this surface roughness does not compromise the material's

intrinsic thermal conductivity, ensuring that the overall efficiency of the heat sink remains intact. Additional smoothing would add complexity and expense to the manufacturing process without providing a proportional improvement in performance [47]. Upon closer inspection, the images depict the grooved channels, highlighting the uniformity and precision achieved during machining. These grooves are more pronounced along the curved sections of the channels, where tool path dynamics and material removal processes play a crucial role. Higher magnification views show a more intricate microstructure, with intersecting patterns possibly resulting from tool oscillations or feed variations. Moreover, the material's response to machining forces can be seen in certain regions, where localised roughness variations are present. The surface roughness of the heat sinks was measured at multiple positions using a Mitutoyo SurfTest SJ-500 profilometer. The roughness values (R_a) were found to vary between $0.36 \mu\text{m}$ and $0.58 \mu\text{m}$, reflecting minor inconsistencies across different sections of the heat sink. These roughness values are within an acceptable range for thermal management applications and indicate that the milling process effectively produced heat sinks with structurally stable fins and channels.

Although the fabrication of the heat sink structures was carried out with careful attention to dimensional accuracy and machining quality, it is important to recognise that even small variations due to manufacturing tolerances and surface roughness can influence thermal and hydraulic performance. Minor deviations in fin height, spacing, or channel width, though within acceptable tolerances, can locally alter the flow distribution, changing Reynolds number and affecting heat transfer uniformity across the heat sink. For example, a slightly narrower flow passage may result in elevated velocity and enhanced local convective heat transfer but also lead to increased pressure drop. Conversely, widened gaps can reduce turbulence intensity and lower thermal performance. These variations also introduce uncertainty when comparing

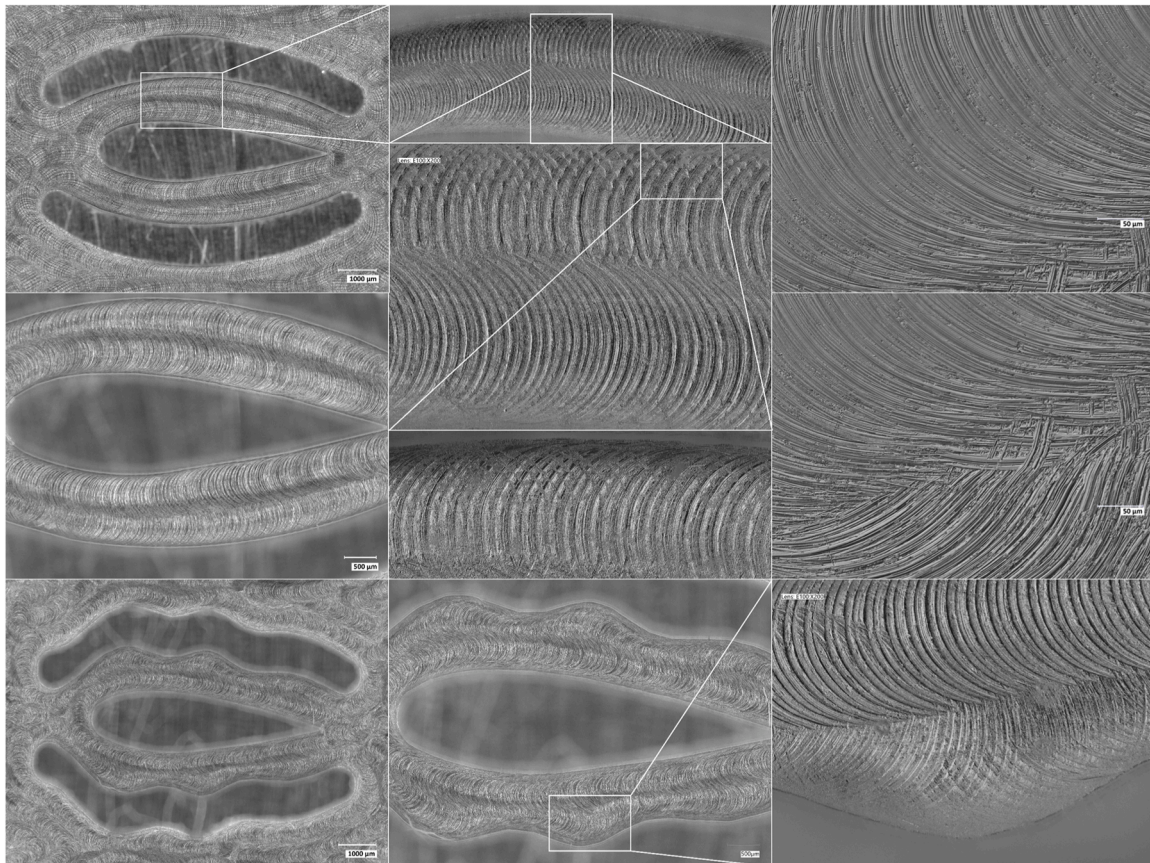


Fig. 5. Scanning Electron Microscope (SEM) images of the fabricated heat sink surfaces showing tool-induced micro-patterns, grooved channels, and surface roughness characteristics. These textures contribute to micro-turbulence and heat transfer enhancement.

closely performing configurations, emphasising the importance of consistent manufacturing practices when scaling up for practical applications.

Surface roughness, resulting from CNC milling, also plays a dual role in system behaviour. On one hand, it can enhance convective heat transfer by disrupting the thermal boundary layer and promoting micro-scale turbulence. On the other hand, it increases wall friction and contributes to higher pumping power requirements. In nanofluid applications, rough surfaces may additionally act as nucleation or adhesion sites for suspended nanoparticles, potentially accelerating sedimentation and fouling under prolonged operation. This can alter local flow dynamics, reduce effective surface area, and compromise long-term reliability. Thus, while the level of roughness observed in this study was beneficial in enhancing thermal transport without introducing excessive pressure loss, future optimisation may involve tuning surface texture or incorporating coatings to balance heat transfer gains with hydraulic efficiency and long-term stability.

3. Experimental setup

To evaluate the thermal and hydraulic performance of heat sinks, an experimental system was designed and assembled, integrating various precision instruments for accurate measurement and temperature control, as shown in Fig. 6(a). The setup featured a storage tank placed within a refrigerated circulator water bath (ARCTIC A40) to maintain a stable and consistent inlet temperature. The coolant was drawn from the storage tank and circulated through the system using a MasterFlex Micro gear pump which ensured a controlled and continuous flow. Next in the loop, a precision flow control valve was installed to manually regulate and stabilize the fluid velocity. Positioned between the needle valve and the heat sink section, a micro-flow meter (Omega FTB332D) was incorporated to accurately measure the flow rate before the fluid entered the inlet manifold.

The heat sink itself was thermally insulated with wool and enclosed within an acrylic plate assembly to minimise heat loss and external

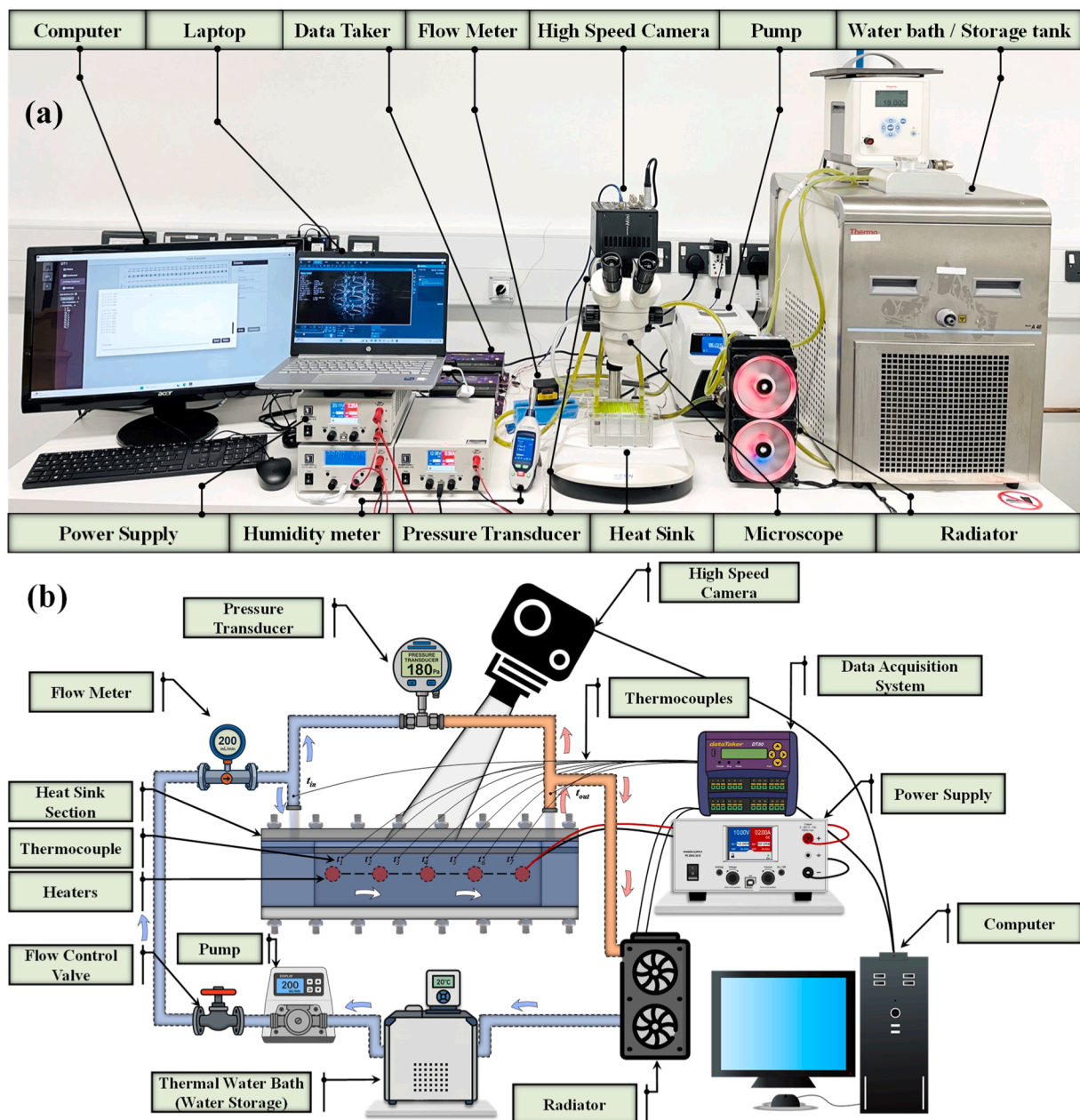


Fig. 6. (a) Experimental test rig used to evaluate the thermal and hydraulic performance of the heat sinks; (b) schematic illustration of the experimental setup.

thermal interference. To facilitate visualization of the coolant flow dynamics and bubble formation within the heat sink channels, a high-speed camera was mounted above the microscope via an adaptor, allowing real-time observation and recording of intricate flow patterns. To ensure a stable and uniform heat input, three cartridge heaters (RS-860–6845, UK) were embedded within the heat sink, powered by a DC supply (EA-PS 2084–10B) to provide the required thermal energy. The pressure drop across the heat sink, a key performance parameter, was measured using a differential pressure transducer (Omega DPGM409–025HDWU, USA). The device was connected at both the inlet and outlet of the heat sink using precision fittings, as illustrated in Fig. 6 (b). This transducer measures gauge pressure with high resolution, enabling accurate assessment of the pressure difference across the mini-channel configuration. The output was logged in real-time through a digital acquisition system.

The working fluid continuously circulated through the micro-channels of the heat sink, effectively absorbing the heat from the heat sink. To monitor the temperature distribution along the heat sink surface, seven K-type thermocouples (RS-397–1589, UK) were embedded at strategic positions along the base of the heat sink channels, positioned just below the wall surface. Additionally, one thermocouple was placed at the fluid inlet and another at the outlet to record the temperature variations at these critical points, ensuring a precise assessment of thermal performance. To ensure reliability and reduce transient noise, the temperature and pressure data were recorded at 5-second intervals over a 30-second period, after achieving steady-state conditions. The average of these readings was then used in subsequent calculations to enhance measurement accuracy.

Following heat absorption in the heat sink, the fluid exited the system and passed through a radiator, which was positioned downstream to dissipate the absorbed heat into the surrounding environment. This radiator played a crucial role in maintaining the thermal balance of the experimental setup by effectively rejecting excess heat. Finally, the coolant completed its cycle by returning to the storage tank, where it was reconditioned to the desired temperature by the refrigerated circulator bath chiller, thereby ensuring a continuous and controlled experimental process.

Through this well-integrated system of components and instrumentation, the setup enabled a rigorous evaluation of the heat sink's performance, allowing for precise measurement and analysis of critical thermal and hydraulic parameters. This experimental configuration provided valuable insights into the efficiency of heat dissipation mechanisms, pressure drop characteristics, and flow behaviour, contributing to the development of optimised cooling solutions for high-performance electronic and thermal management applications.

4. Nanofluid synthesis, characterisation, and thermophysical properties

The nanofluids employed in this study have been extensively investigated in our prior research, where their preparation methods, stability characteristics, and thermophysical properties were comprehensively detailed [48]. A brief overview is provided here to avoid redundancy and maintain clarity. The nanofluids comprise Ag, BeO, and SiC nanoparticles dispersed in water, either individually or in hybrid formulations. The average particle sizes were 10–40 nm for Ag, 45–55 nm for SiC (beta-phase), and 85–140 nm for BeO, as determined by transmission electron microscopy and verified by supplier specifications. These materials were selected based on a comprehensive evaluation of their thermal conductivity, density, stability characteristics, and economic feasibility, with the objective of optimising heat transfer efficiency in cooling applications.

4.1. Preparation of nanofluids

A two-step method was employed to prepare both unitary and hybrid nanofluids. Initially, the calculated amount of nanoparticles was dispersed into distilled water while performing magnetic stirring for 1 h. This was followed by bath sonication for 2 h and subsequent probe ultrasonication for 15 min to ensure a uniform suspension and break down any agglomerates. For hybrid formulations (Ag/SiC, Ag/BeO, and SiC/BeO), individual nanofluid suspensions were prepared separately and then combined in predetermined volumetric ratios, with an additional round of probe ultrasonication for 15 min to achieve homogeneity.

To counteract the natural tendency for nanoparticles to aggregate, surfactants were incorporated during the preparation process. Among the various surfactants investigated, Sodium Dodecylbenzene Sulfonate (SDBS) consistently provided the best stability by promoting both electrostatic and steric repulsion among particles. This approach also influenced the pH of the suspension, which is crucial for maintaining optimal repulsive interactions.

4.2. Structural and morphological characterisation

The crystallographic properties and phase compositions of the nanoparticles were confirmed using X-ray Diffraction (XRD). Analysis revealed well-defined diffraction peaks corresponding to the face-centered cubic structure of silver, the hexagonal wurtzite phase of BeO, and the cubic/orthorhombic structure of SiC. The average crystallite sizes were estimated to be approximately 16.6 nm for Ag, 23.1 nm for BeO, and 17.2 nm for SiC.

Transmission Electron Microscopy (TEM) provided further insights into particle morphology. The TEM images highlighted distinct characteristics: Ag nanoparticles were predominantly spherical and tended to form clusters, BeO nanoparticles exhibited irregular, hexagonal shapes, and SiC nanoparticles showed a variety of shapes with a notable tendency to form chain-like agglomerates. In hybrid nanofluids, the intermixing of different nanoparticle types appeared to reduce the overall agglomerate size, suggesting a synergistic effect that enhances dispersion.

4.3. Stability and dispersion analysis

The stability of the nanofluids was rigorously evaluated using both visual inspection and zeta potential measurements. Samples were monitored over a period of four weeks to assess the sedimentation or agglomeration. Zeta potential values observed to be varied from –45 to –75 mV, which confirm a high level of stability. Additionally, dynamic light scattering analysis indicated that in hybrid formulations, the synergistic interactions between different nanoparticles were found to reduce the tendency for large agglomerate formation, further contributing to a stable dispersion over time.

4.4. Thermophysical properties

The thermophysical properties of the nanofluids were evaluated over a range of temperatures. Thermal conductivity was measured using the transient plane source (TPS) technique via the Hot Disk 2500S Thermal Constants Analyzer. This system employs a sensor with a double spiral configuration encapsulated in a thin Kapton layer, designed to serve both as a heat source and a resistance thermometer. The sensor, with a radius of 2.001 mm, operated at a heating power of 60 mW over a 2-second interval, enabling precise determination of thermal conductivity at various temperatures.

Dynamic viscosity was determined using a Brookfield viscometer (DVNext Cone/Plate Rheometer). This device measures the resistance of the nanofluid to shear and captures subtle changes in viscosity due to nanoparticle incorporation, ensuring that the fluid retains effective convective heat transfer properties.

Density measurements were performed with a calibrated densitometer (Anton Paar DMA 35), which accurately detected the small increases in density associated with low nanoparticle loadings. These modest density augmentations contribute to the overall thermal performance without adversely affecting fluid dynamics.

- 1. Thermal Conductivity:** Measurements using the transient plane source (TPS) technique revealed that thermal conductivity improvements ranged from 5.31% to 7.43% depending on the specific hybrid combination and mixing ratio. For example, the Ag/SiC (60:40) formulation demonstrated an enhancement of approximately 7.43%, whereas Ag/BeO (60:40) and SiC/BeO (80:20) exhibited enhancements of around 7.17% and 5.31%, respectively.
- 2. Viscosity:** While the incorporation of nanoparticles led to a slight increase in viscosity, the nanofluids maintained Newtonian behaviour. A minimum viscosity enhancement of about 3.01% was noted for the BeO nanofluid, with hybrid Ag/SiC formulations showing a maximum enhancement of up to 4.90% for certain mixing ratios.
- 3. Density:** Density measurements indicated modest increases, with maximum augmentations of approximately 0.25%, 0.097%, and 0.0775% for Ag, SiC, and BeO nanofluids, respectively, at a concentration of 0.025 vol%. In hybrid formulations, the Ag/SiC system exhibited a maximum density increase of about 0.23% for the 80:20 composition.

To predict the values, empirical models were developed for thermal conductivity, viscosity, and density as functions of temperature. Additionally, the heat capacity of the nanofluids was evaluated using the Xuan and Roetzel model [49], which accounts for the contributions of both the base fluid and the nanoparticles.

These nanofluids were integrated into the heat sink system to improve heat dissipation efficiency. The combination of high thermal conductivity, controlled viscosity, and stable dispersion makes them well-suited for applications in electronic cooling, where efficient thermal management is critical. The synergistic effects observed in hybrid nanofluids provide an optimal balance between performance enhancement and cost considerations, making them a viable solution for advanced heat sink designs.

4.5. Safety, environmental, and practical considerations

The nanoparticles used in this study were selected based on their thermal performance characteristics, including conductivity, dispersion stability, and compatibility with water-based systems. While Ag and SiC are generally regarded as safe at low concentrations and when handled in liquid suspension, BeO poses greater concern due to its known toxicity in powder form, particularly via inhalation [50–52]. To ensure safety, all nanofluids were prepared and handled exclusively in liquid form within a controlled laboratory setting. Appropriate precautions including the use of fume hoods, sealed containers, and personal protective equipment (PPE) were strictly followed during all stages of preparation and testing. Additionally, instrument selection and experimental conditions were carefully controlled to minimise any risk of exposure. These additional safety measures, along with future end-of-life disposal requirements, contribute to slightly higher preparation and operational costs when working with nanomaterials.

In real-world applications, these nanofluids operate within closed-loop cooling systems, where the working fluid is fully contained, eliminating direct human or environmental exposure during operation.

Under such conditions, the nanoparticles remain suspended in the liquid and circulate continuously through the system without contact with external surfaces. However, when decommissioning or replacing such systems, proper disposal practices are essential. Devices containing nanofluids, especially those with BeO should be treated as hazardous waste and disposed of through certified channels in compliance with environmental and safety regulations. With these measures in place, the high thermal performance offered by nanofluid-enhanced cooling systems can be leveraged without compromising safety or environmental responsibility.

5. Data processing

During the experimental campaign, data was collected at regular intervals to capture the thermal performance of the liquid-cooled heat sink. The measured data included the inlet and outlet temperatures of the working fluid, as well as the temperatures at specific positions within the heat sink. In addition, essential flow parameters such as volumetric flow rate, pressure drop across the heat sink, and the input electrical power used to generate heat were continuously monitored and recorded. To analyse the experimental results obtained from the experimental study, several equations and calculations were employed to determine various parameters related to heat transfer and thermal performance.

The mass of nanoparticles (m_{np}) added to the base fluid was calculated using a mass balance approach based on the particle volume fraction (φ). This well-established method, frequently cited in the literature [53,54], considers the relative densities of both the nanoparticles and the base fluid, as expressed in Eq. (1).

$$\varphi = \left[\frac{\frac{m_{np}}{\rho_{np}}}{\frac{m_{np}}{\rho_{np}} + \frac{m_{bf}}{\rho_{bf}}} \right] \quad (1)$$

5.1. Hydraulic diameter calculations

Hydraulic diameter is a key geometric parameter that characterises the flow passage in channels with non-uniform cross sections. In conventional channels, the hydraulic diameter (d_h) is defined as four times the cross-sectional area divided by the wetted perimeter. However, when the channel cross section varies along its length, as this study used airfoil integrated curvilinear and corrugated curvilinear pin-fin heat sinks, this simple model no longer adequately represents the effective flow area. A modified approach is therefore used to account for these variations, following techniques reported in the literature [22,55,56].

To compute the hydraulic diameter for a channel with varying cross-sectional area, Eqs. (2)–(4) is used:

$$V_{sec} = (L \times W - A_{fin,top})H \quad (2)$$

$$S_{sec} = (P_{fin} \times H) + 2(L - L_{a,fin})H + (L \times W - A_{fin,top}) \quad (3)$$

$$d_h = \frac{4V_{sec}}{S_{sec}} \quad (4)$$

In these equations, V_{sec} denoted the volume of the specific sections shown in Fig. 7, while L , W , and H symbolised the length, width, and height, respectively. $A_{fin,top}$ is the top surface area of the fin that is subtracted from the overall section area. S_{sec} represents the effective side surface area or wet area, which accounts for the contributions of the fin's lateral surfaces as well as the remaining section area. P_{fin} and $L_{a,fin}$ denoted the effective perimeter and length of the airfoil fin. By using these equations, the hydraulic diameter d_h is determined in a way that reflects the actual flow constraints imposed by the non-uniform channel geometry, ensuring a more accurate prediction of fluid flow, and heat transfer characteristics in such complex configurations.

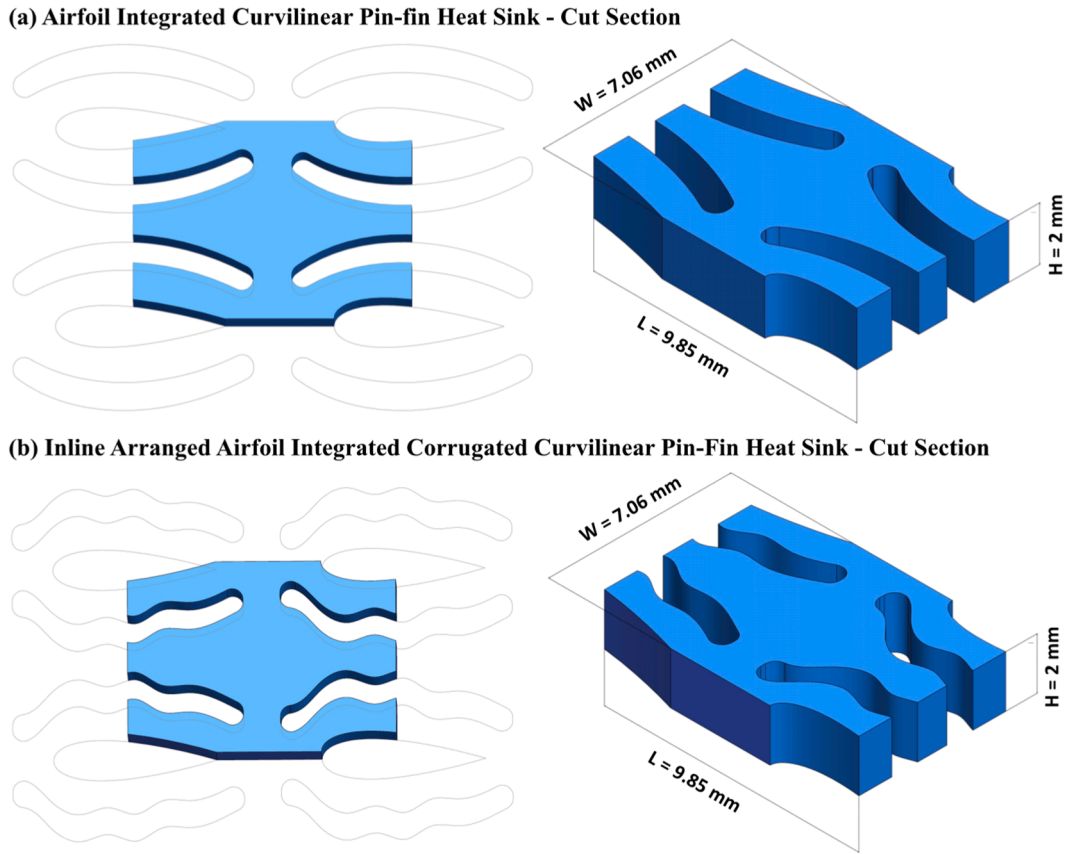


Fig. 7. Cut sections and dimensional details of the IACPF (top) and AICCPF (bottom) heat sink configurations.

5.2. Performance parameters

The performance parameters are quantified through a series of equations that relate the thermal and flow characteristics of the system.

The mean bulk temperature (T_{mean}) is calculated using Eq. (5) as the arithmetic average of the inlet and outlet temperatures.

$$T_{mean} = \frac{T_{inlet} + T_{outlet}}{2} \quad (5)$$

This equation provides an average temperature of the fluid, representing its thermal state as it flows through the channel.

The rate of heat transfer (\dot{Q}) is determined using Eq. (6).

$$\dot{Q} = \dot{m}C_p(T_{outlet} - T_{inlet}) \quad (6)$$

Here, \dot{m} is the mass flow rate and C_p is the specific heat capacity of the fluid. This expression quantifies the heat absorbed by the fluid as it passes through the heat sink.

The channel wall temperature (T_w) is estimated by applying Eq. (7).

$$T_w = T_b - \left(\frac{\dot{Q}l_x}{k_s A_w} \right) \quad (7)$$

In this equation, T_b is the base temperature, l_x is the distance from the base to the channel wall, k_s is the thermal conductivity of the heat sink material, and A_w is the wall surface area. It models the temperature drop across the wall due to conduction. However, the wall surface area (A_w) is computed using Eq. (8).

$$A_w = L_s \times W_s \quad (8)$$

L_s and W_s are the length and width of the heat sink's finned area, respectively.

Since the temperature difference between the wall and the fluid is not constant along the flow direction, the logarithmic mean temperature

difference ($LMTD$) is used, calculated by Eq. (9) [57–59].

$$LMTD = \frac{(T_w - T_{inlet}) - (T_w - T_{outlet})}{\ln \left[\frac{(T_w - T_{inlet})}{(T_w - T_{outlet})} \right]} \quad (9)$$

Here, $LMTD$ provides an effective average temperature difference that drives the heat transfer process.

The convective heat transfer coefficient (h) is derived from the rate of heat transfer and the effective temperature difference using Eq. (10):

$$h = \left[\frac{\dot{m}C_p(T_{outlet} - T_{inlet})}{A_{seff} \times (LMTD)} \right] \quad (10)$$

A_{seff} is the effective area over which convection takes place, and this coefficient indicates the efficiency of convective heat removal.

The Reynolds number (Re) is a dimensionless parameter that characterises the flow regime, calculated using Eq. (11) [60].

$$Re = \frac{\rho v d_h}{\mu} \quad (11)$$

In this equation, ρ is the fluid density, v is the average velocity, d_h is the hydraulic diameter, and μ is the fluid viscosity.

The average velocity (v) of the fluid is obtained by dividing the volumetric flow rate (q) by the cross-sectional area, determined using Eq. (12). However, the average cross-sectional area (A_{avg}) of the channel is calculated with Eq. (13).

$$v = q/A_{avg} \quad (12)$$

$$A_{avg} = \frac{V_{sec}}{L} \quad (13)$$

Here, V_{sec} represents the effective volume of the specific flow section, and L is the length.

Thermal resistance (R_{th}) is an inverse measure of the system's heat transfer efficiency and is given by Eq. (14) [61]. A lower thermal resistance indicates a more effective heat transfer process.

$$R_{th} = \frac{LMTD}{\dot{Q}} \quad (14)$$

The Nusselt number (Nu) is a dimensionless indicator of convective heat transfer enhancement over pure conduction, calculated using Eq. (15):

$$Nu = \frac{hd_h}{k_c} \quad (15)$$

Here, k_c is the thermal conductivity of the coolant. A higher Nu signifies improved convective performance.

The pumping power (PP) required to circulate the fluid is estimated using Eq. (16).

$$PP = q \times \Delta P \quad (16)$$

In this equation, q is the volumetric flow rate and ΔP is the pressure drop across the channel. This parameter is important for evaluating the energy cost of fluid circulation.

Finally, the Darcy friction factor (f) is calculated using Eq. (17):

$$\frac{U_h}{h} = \sqrt{\left(\frac{U_m}{m}\right)^2 + \left(\frac{U_{(T_w-T_i)}}{(T_w-T_i)}\right)^2 + \left(\frac{U_{(T_w-T_o)}}{(T_w-T_o)}\right)^2 + \left(\frac{U_{C_p}}{C_p}\right)^2 + \left(\frac{U_{A_{eff}}}{A_{eff}}\right)^2 + \left(\frac{U_{(T_{out}-T_{in})}}{(T_{out}-T_{in})}\right)^2} \quad (21)$$

$$f = \frac{2\Delta P d_h}{\rho L v} \quad (17)$$

Each equation plays a critical role in the overall analysis of the heat sink's performance, linking the thermal and hydrodynamic characteristics to the design and operational parameters. Together, they provide a comprehensive framework for assessing the effectiveness of the cooling system.

Uncertainty analysis is a critical aspect of micro- and mini-scale experiments, ensuring the accuracy and reliability of experimental findings while carefully assessing the errors associated with measuring instruments. To quantify the uncertainties in various measured parameters, the study adopted an approach consistent with methodologies employed by other researchers. This rigorous analysis enhances confidence in the experimental data and improves the precision of the reported results.

The uncertainties in different parameters were determined using a set of established equations, specifically Eqs. (18)–(22). The analysis revealed that the maximum uncertainties for the Reynolds number, hydraulic diameter, and Nusselt number were 6.18%, 1.63%, and 6.26%, respectively. These values indicate an acceptable level of

accuracy in the measurements. Additionally, Table 2 presents the accuracy specifications of the instruments used in the study.

To further ensure the reliability of the measurements, repeat trials were conducted at selected flow rates and heating powers. The results showed strong consistency across these trials, with variations in the Nusselt number remaining within $\pm 2\%$, and pressure drop variations within $\pm 4\%$ for water-based tests. However, in the case of nanofluids, the variability was slightly higher, observed within $\pm 3.5\%$ for Nusselt number and $\pm 6\%$ for pressure drop. These findings reinforce the stability of the test rig and the repeatability of the experimental methodology.

$$\frac{U_{d_h}}{d_h} = \sqrt{\left(\frac{U_h}{h}\right)^2 + \left(\frac{U_w}{w}\right)^2} \quad (18)$$

$$\frac{U_v}{v} = \sqrt{\left(\frac{U_{d_h}}{d_h}\right)^2 + \left(\frac{U_m}{m}\right)^2 + \left(\frac{U_A}{A}\right)^2} \quad (19)$$

$$\frac{U_{Re}}{Re} = \sqrt{\left(\frac{U_\rho}{\rho}\right)^2 + \left(\frac{U_v}{v}\right)^2 + \left(\frac{U_\mu}{\mu}\right)^2} \quad (20)$$

$$\frac{U_{Nu}}{Nu} = \sqrt{\left(\frac{U_h}{h}\right)^2 + \left(\frac{U_{d_h}}{d_h}\right)^2 + \left(\frac{U_{k_f}}{k_f}\right)^2} \quad (22)$$

6. Results and discussion

6.1. Validation

The experimental test rig was validated through a series of experiments using a specially designed and fabricated aluminium straight channel heat sink. The selection of this specific configuration was driven by its widespread use in thermal management applications and the availability of extensive literature on its thermal and fluidic performance. This approach was used as the heat sink designs explored in this study have not been previously investigated, and no prior experimental data exists for direct comparison. Therefore, employing a well-characterised conventional heat sink facilitated the benchmarking of experimental results against established theoretical and numerical predictions. In addition, the straight channel heat sink provided the advantage of having classical models available for predicting the Nusselt number. In this study, the experimental results were compared with the model developed by Shah et al. [62], which is widely accepted for predicting Nusselt numbers in laminar flow under constant heat flux boundary conditions. The Shah model provides a theoretical foundation for evaluating the convective heat transfer performance in ducts of various geometries, including parallel plates, circular tubes, and non-circular channels. In the present work, this model serves as a validation benchmark to compare against the experimentally obtained Nusselt numbers using a conventional straight-channel heat sink under identical boundary conditions. The choice of this model is justified due to its extensive application in previous heat transfer literature [63–66], particularly for evaluating microchannel and mini-channel systems

Table 2
Accuracy and measurement range of experimental instruments.

Instrument	Accuracy	Operational Range
Flow Sensor	$\pm 6\%$	0.1 – 1 l/min
Temperature Probe	$\pm 1.5\text{ }^\circ\text{C}$	–75 to 260 $^\circ\text{C}$
Pressure Gauge	$\pm 0.08\%$ BSL (incl. linearity, hysteresis, repeatability) and $\pm 0.15\%$ for analogue output	0 – 25 mbar
DC Power Supply	Current: $< 0.3\%$ Voltage: $< 0.2\%$	0 – 10 A 0 – 84 V

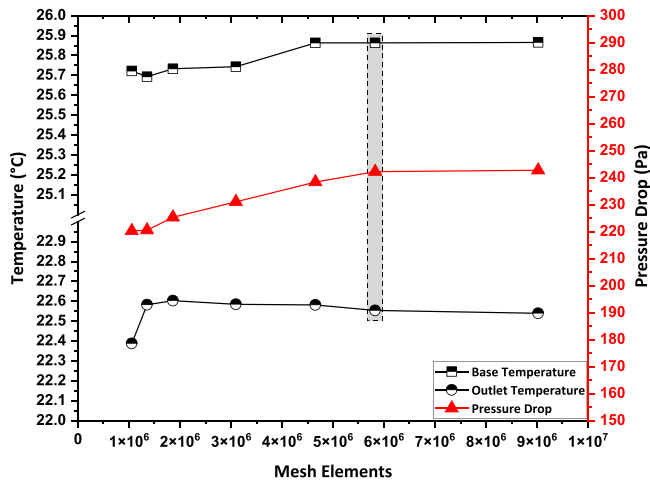


Fig. 8. Variation of wall temperature, outlet temperature, and pressure drop with respect to mesh element count, mesh independence study for the straight-channel heat sink.

operating under laminar regimes. The good agreement between the experimental data and Shah’s prediction validates the reliability of the test rig and confirms the accuracy of the measured thermal performance parameters. Additionally, a computational fluid dynamics (CFD) analysis was performed using ANSYS Fluent to further validate the experimental findings.

The experimental tests were carried out by varying the Reynolds number within the range of 100–300 while maintaining a constant heating power of 100 W. The obtained Nusselt number values were then compared with those predicted by the Shah model, Eq. (23). Furthermore, a detailed CFD simulation was conducted to replicate the experimental conditions, and a mesh independence study was performed to optimise the accuracy of the numerical results. The simulations aimed to replicate the experimental conditions and assess the accuracy of the test rig through comparison of Nusselt number and temperature profiles. The steady-state forms of the continuity, momentum, and energy equations were solved to model laminar flow through the channels, as the maximum Reynolds number remained below 1000 across all test cases. The laminar flow model was therefore deemed appropriate and computationally efficient for this flow regime.

Pressure-velocity coupling was handled using the Semi-Implicit Method for Pressure-Linked Equations (SIMPLE) scheme, which

provides stable convergence for incompressible, laminar flows. For spatial discretisation, a second-order upwind scheme was used for all transport equations to ensure greater numerical accuracy, especially in resolving thermal gradients. The flux type was set to distance-based, which enhances precision in capturing interfacial behaviour, particularly in conjugate heat transfer problems.

The mesh refinement process considered variations in base temperature, outlet temperature, and pressure drop, ensuring that the numerical model provided a reliable representation of the physical experiment. The outcomes of the mesh independence study, including the effects of mesh refinement on base temperature, outlet temperature, and pressure drop, are depicted in Fig. 8.

To quantitatively assess the deviation between experimental results and predictions from both the theoretical model and CFD simulations, the mean absolute error (MAE) was calculated using Eq. (24) [67,68]. The MAE serves as an effective measure of the average magnitude of the discrepancies between experimental and predicted values, offering insight into the consistency and accuracy of the validation process.

The results of the validation study demonstrated that the experimental data closely aligned with the theoretical predictions, with an MAE of 2.76% when compared to the Shah model. This low error margin underscores the reliability of the experimental test rig and the accuracy of the data acquisition process. However, when comparing the experimental results with the CFD simulations, a slightly higher MAE of approximately 5.7% was observed, as illustrated in Fig. 9. A closer inspection of the data revealed that the agreement between experimental and CFD results was strongest at lower flow rates, while deviations increased as the Reynolds number rose. This discrepancy at higher flow rates may be attributed to factors such as minor experimental uncertainties, limitations in numerical turbulence modelling, or variations in thermal boundary conditions that were not fully captured in the CFD model. The validation study confirms the robustness of the experimental setup, demonstrating its capability to produce reliable and reproducible results.

$$Nu = \begin{cases} 1.953 \left(Re Pr \frac{d_h}{l} \right)^{1/3} & \text{if } \left(Re Pr \frac{d_h}{l} \right) \geq 33.3 \\ 4.364 + 0.0722 \left(Re Pr \frac{d_h}{l} \right) & \text{if } \left(Re Pr \frac{d_h}{l} \right) < 33.3 \end{cases} \quad (23)$$

$$\text{Mean Absolute Error (MAE)} = \frac{1}{n} \sum_{j=1}^n \left[\frac{|x_{exp.} - x_{pred.}|}{x_{exp.}} \right] \times 100\% \quad (24)$$

In these equations, l represents the finned section length, Pr is the Prandtl number, and d_h denotes the hydraulic diameter. The variable n refers to the total number of data points, while $x_{exp.}$ and $x_{pred.}$ correspond to the experimental and predicted values, respectively.

6.2. Comparative study

To evaluate the potential of the proposed heat sink design, a comparative study was conducted against a conventional straight-channel heat sink under identical experimental conditions. The experiments were carried out across a range of flow rates, varying from 200 mL/min to 450 mL/min, while maintaining a constant heating power of 150 W. The results demonstrated that the AICCPF heat sink achieved a twofold enhancement in Nusselt number compared to the conventional straight-channel heat sink. At the highest flow rate, the Nusselt number increased from 7.60 to 15.5, indicating an approximately 103% improvement in heat transfer efficiency, as presented in Fig. 10(a). This substantial enhancement is attributed to the biomimetic-inspired channel geometry, which optimises convective heat transfer by promoting more effective fluid mixing and surface interaction. Additionally, while the improved heat transfer characteristics were evident, the study also noted a corresponding increase in pressure drop. The measured pressure drop across the AICCPF heat sink was found to be

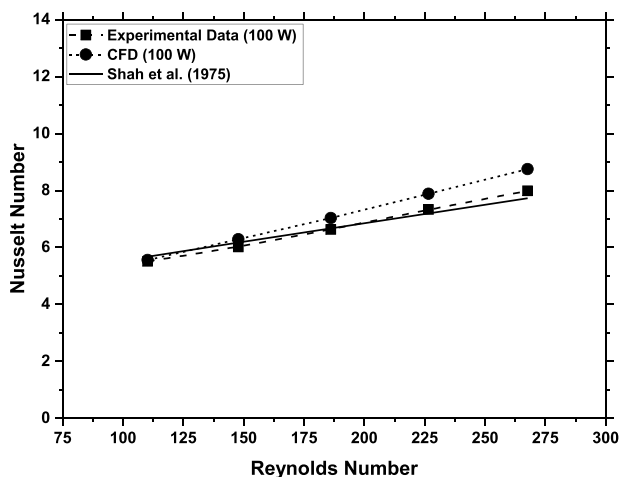


Fig. 9. Validation of experimental results using Shah’s model and CFD simulations across varying Reynolds numbers, confirming the reliability of the test rig.

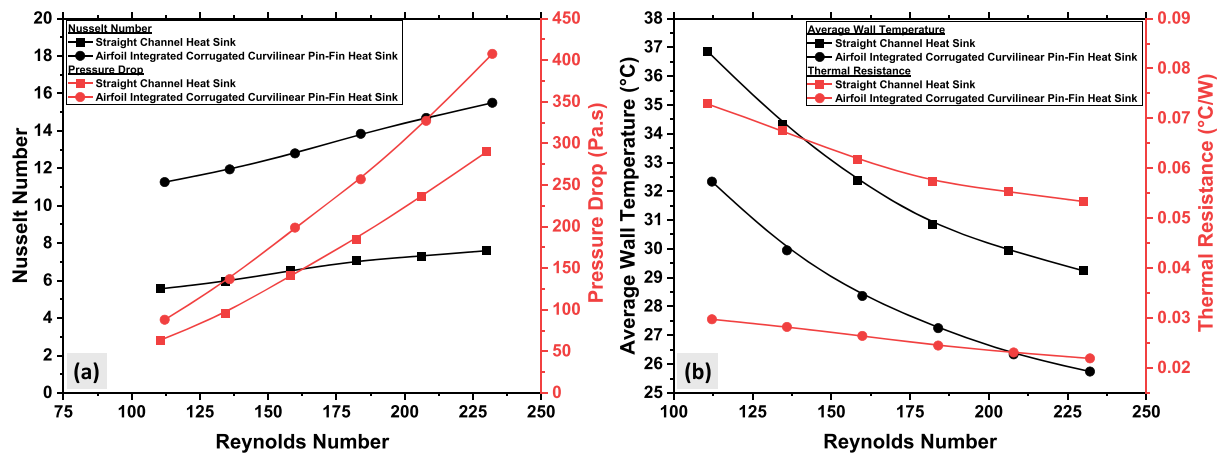


Fig. 10. Comparison of thermal and hydraulic performance parameters for the AICCPF and conventional straight-channel heat sink.

37.5% higher than that of the conventional straight-channel design.

One of the most significant observations was the impact of the proposed design on thermal resistance. As anticipated, the improved heat dissipation characteristics of the AICCPF heat sink led to a notable reduction in both the average wall temperature and thermal resistance. The enhanced surface area facilitated more efficient heat transfer, lowering the average wall temperature by up to 4.52 °C. This improvement directly contributed to a significant reduction in thermal resistance, with an average decrease of 138.1% compared to the straight-channel heat sink, as illustrated in Fig. 10(b). The optimised thermal performance of the proposed design underscores its effectiveness in maintaining lower operating temperatures while efficiently managing heat dissipation.

The findings of this study underscore the potential of the proposed biomimetic heat sink design for next-generation thermal management applications, particularly in high-performance electronics and AI-driven systems. The integration of AICCPF offers an optimised balance between heat dissipation and fluid flow resistance, making it a promising solution for advanced cooling technologies.

6.3. Nusselt number

The Nusselt number, a key dimensionless indicator of convective heat transfer efficiency, was evaluated for the Inline Arranged Airfoil Integrated Curvilinear Pin-Fin (IACPF) and Inline Arranged Airfoil Integrated Corrugated Curvilinear Pin-Fin (AICCPF) heat sinks. It was determined using both simple and hybrid nanofluids across a range of heating powers and plotted as a function of Reynolds number (Re), as shown in Fig. 11. The comparative study demonstrated that AICCPF exhibited superior heat transfer characteristics compared to IACPF. Additionally, among the tested working fluids, the hybrid nanofluid comprising Ag and SiC nanoparticles outperformed all other samples, delivering enhanced heat transfer performance. The results indicated a direct correlation between the Nusselt number, Reynolds number, and heating power. The minimum Nusselt number values were observed at the lowest Reynolds number and heating power, while the maximum values were recorded at the highest Reynolds number and heating power considered in this study. This trend aligned with fundamental heat transfer principles, as higher flow rates and increased thermal input contributed to greater convective heat transfer, reducing the thermal boundary layer thickness and enhancing heat dissipation [69]. A key factor contributing to the superior performance of AICCPF over IACPF is the integration of corrugated pin-fins. The unique corrugated shape not only provides a more efficient surface area for heat dissipation compared to the simple curvilinear pin-fins but also introduces localised flow disturbances, which promote enhanced fluid mixing and improve the

overall heat transfer process [70]. Using water as the working fluid, the AICCPF configuration exhibited a maximum Nusselt number enhancement of 10.23% compared to IACPF at a heating power of 75 W.

As the geometrical configuration of pin-fins significantly improved heat transfer, the utilization of advanced thermal coolants further enhanced this effect [71]. Among the simple nanofluids tested, Ag nanofluid exhibited the most significant improvement in Nusselt number, increasing from 10.50 to 16.47 in the IACPF configuration and from 11.31 to 18.53 in AICCPF, as both Reynolds number and heating power increased. These enhancements represent a substantial gain in heat transfer efficiency, highlighting the synergy between nanofluid properties and flow-optimised biomimetic designs. In comparison, SiC nanofluid showed slightly better performance than BeO, though both were less effective than Ag nanofluid. For SiC, the Nusselt number ranged from 10.3 to 15.9 in the IACPF and from 11.1 to 17.2 in the AICCPF configuration as the heating power increased from 75 W to 300 W. BeO nanofluid yielded the lowest values, with a peak Nusselt number of 15.5 in IACPF and 16.9 in AICCPF at 300 W. These differences are primarily attributed to the lower thermal conductivity of SiC and BeO relative to Ag, which limits their overall heat transfer enhancement potential despite good dispersion stability.

The observed heat transfer enhancement with nanofluids can be attributed to several mechanisms. The inclusion of nanoparticles increases the effective thermal conductivity of the base fluid, allowing more efficient energy transport. Additionally, Brownian motion of the nanoparticles induces micro-convection within the fluid, disrupting the thermal boundary layer and promoting enhanced heat transfer at the solid-liquid interface [72,73]. Particle-fluid interactions, particularly in the presence of well-dispersed and thermally conductive materials like Ag, further improve the uniformity of temperature distribution across the channel walls. These combined effects explain the superior performance of nanofluid-cooled biomimetic heat sinks compared to water alone.

Hybrid nanofluids exhibited superior thermal performance, with Ag/SiC achieving the highest Nusselt number values among all tested samples. This improvement was attributed to the enhanced suspension stability of hybrid nanofluids and the synergistic effects of different nanoparticles [74]. The presence of both Ag and SiC particles resulted in improved thermal conductivity and effective heat dissipation. Specifically, for the Ag/SiC hybrid nanofluid, the Nusselt number ranged from 10.87 to 16.94 with IACPF and from 11.81 to 18.35 with AICCPF. The Ag/BeO hybrid nanofluid closely followed the performance of Ag/SiC, with values fluctuating near those of the Ag nanofluid. Meanwhile, the SiC/BeO hybrid nanofluid exhibited comparatively lower Nusselt number values due to the inherently lower thermal conductivity of its constituent nanoparticles. However, this composition could be preferred

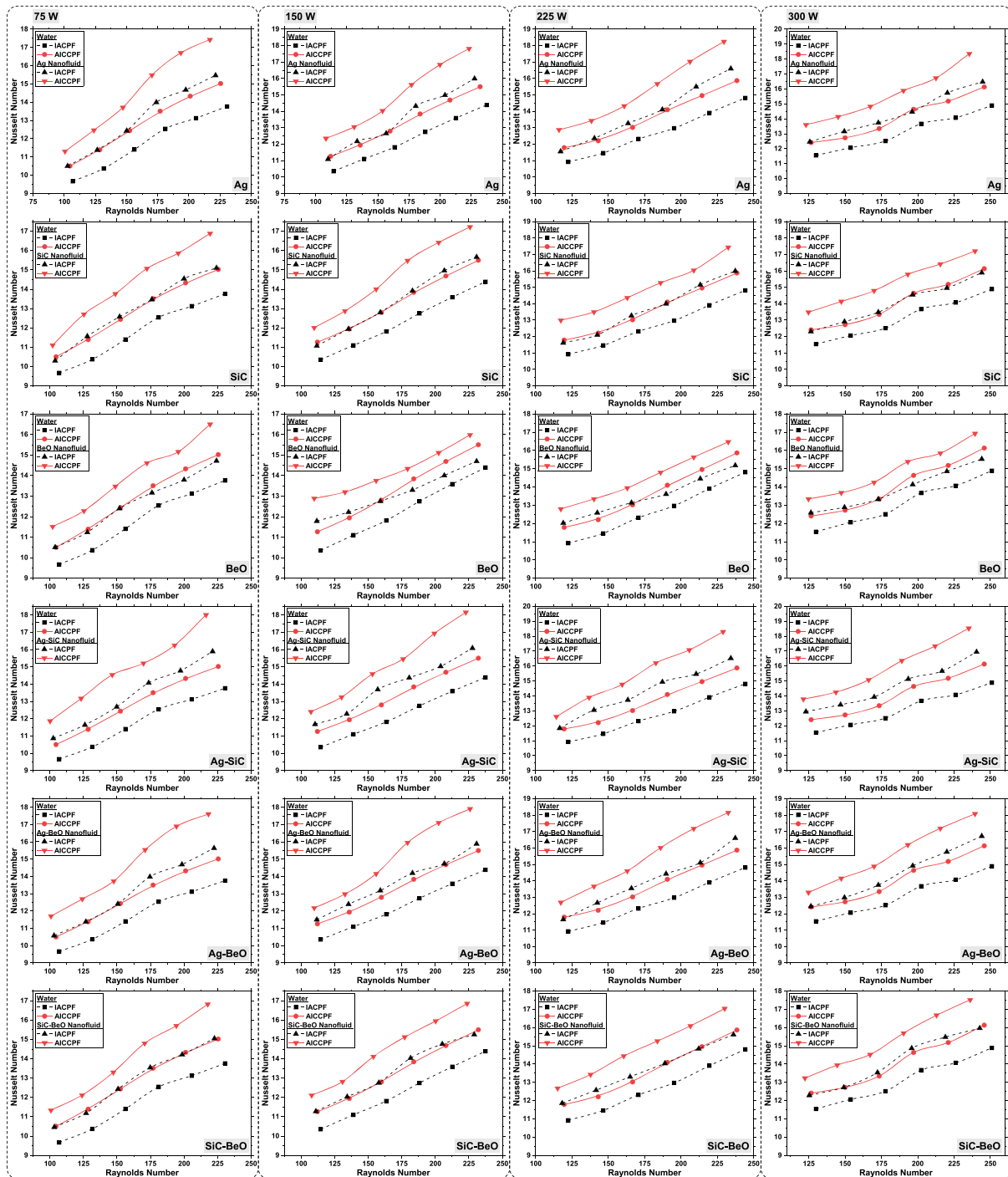


Fig. 11. Variation of Nusselt number with Reynolds number for the IACPF and AICCPF heat sink configurations under different heating powers using water, mono nanofluids (Ag, SiC, BeO), and hybrid nanofluids (Ag/SiC, Ag/BeO, SiC/BeO).

in cost-sensitive applications, as both SiC and BeO were significantly more economical than Ag.

An important observation in this study was the behaviour of nanoparticles concerning sedimentation and agglomeration inside the heat sink channels. On a microscopic level, particle deposition on surfaces could have both positive and negative effects on heat transfer. Some particles may settle within micro-gaps, reducing the effective heat transfer surface area while simultaneously decreasing flow resistance by smoothing out roughness. Conversely, excessive particle accumulation on channel surfaces could increase flow resistance, potentially affecting heat transfer either positively by increasing contact area or negatively

by restricting direct fluid contact with the surface [75].

However, differences in nanoparticle densities led to distinct sedimentation behaviour. For instance, Ag nanoparticles, which had a density approximately three times higher than SiC and BeO, were more prone to settling inside the channels. BeO nanoparticles, due to their relatively larger size compared to Ag and SiC, showed a pronounced tendency to agglomerate, forming clusters that were difficult to disperse. In contrast, SiC nanoparticles primarily formed chain-like agglomerates, which were easier to break and remix into the fluid, even at higher flow rates. As shown in Fig. 12, where it was evident that SiC particles did not agglomerate and form large clusters like Ag and BeO.

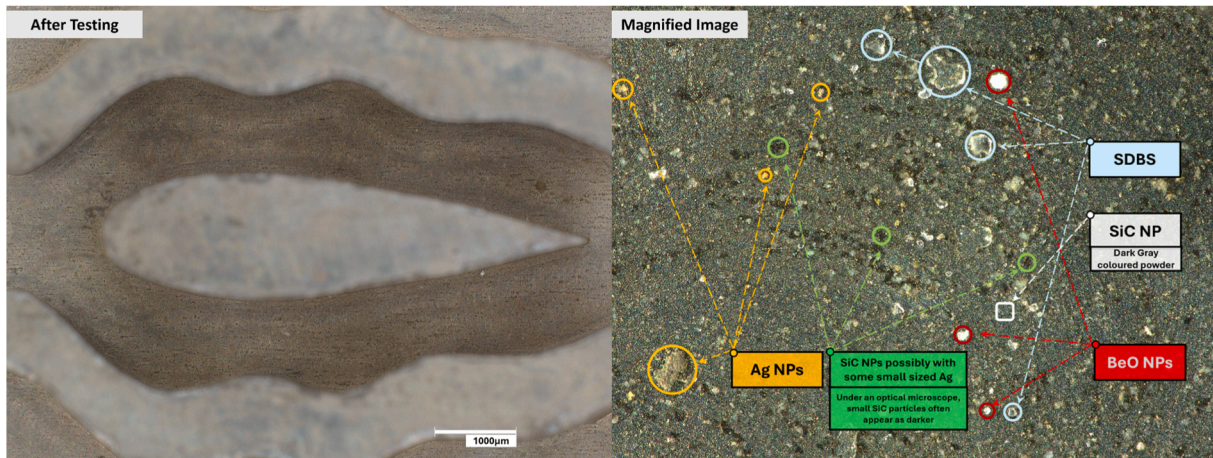


Fig. 12. Microscopic observation of nanoparticle sedimentation and agglomeration inside the heat sink channels.

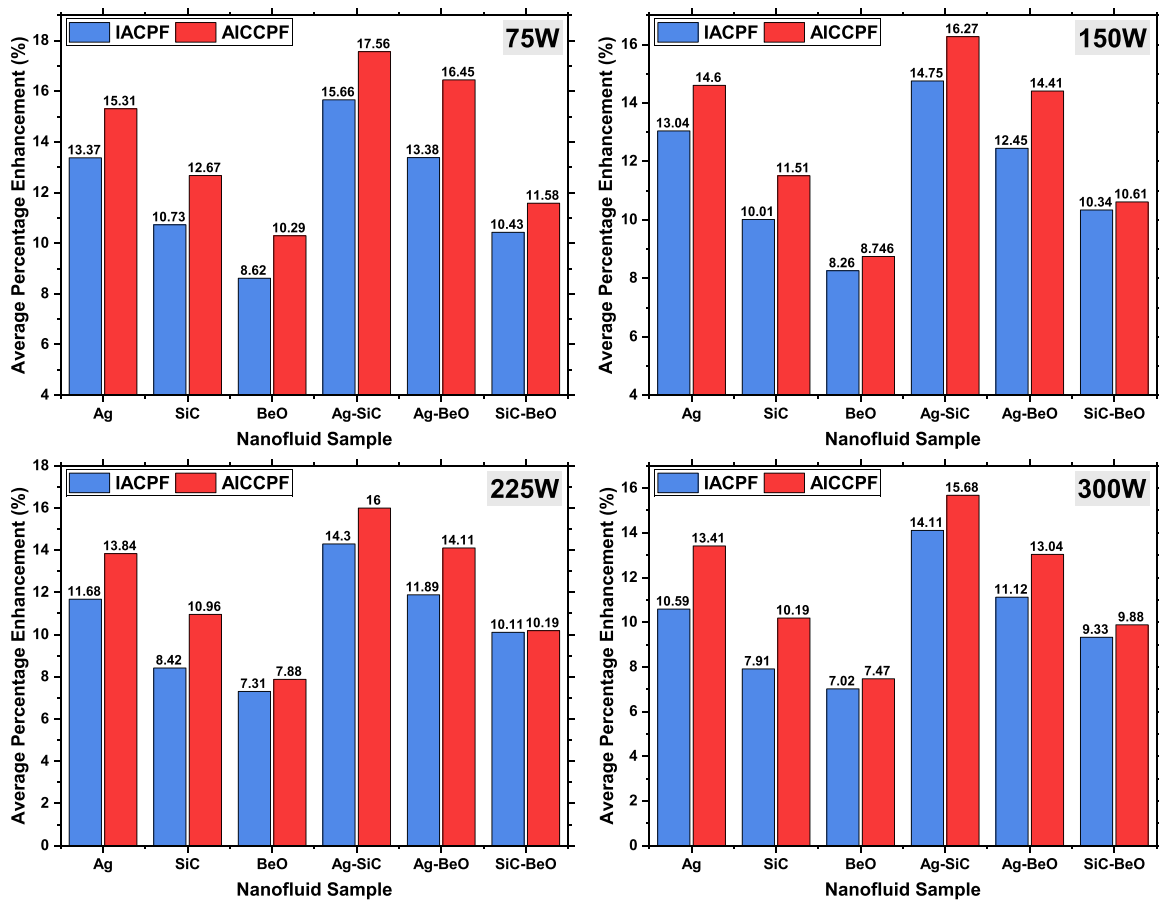


Fig. 13. Average percentage enhancement in Nusselt number for various mono and hybrid nanofluids relative to water, evaluated for both IACPF and AICCPF configurations at different heating powers (75 W, 150 W, 225 W, and 300 W).

The role of surfactants in nanofluid stability could also not be overlooked. In this study, sodium dodecyl benzene sulfonate (SDBS) was used as a surfactant to improve dispersion. However, as the heat sink continuously experiences high thermal loads, surfactant accumulation on surfaces could negatively impact heat transfer efficiency due to the inherently lower thermal conductivity of surfactant materials.

For mini and micro-channel heat sinks, prolonged use of nanofluids may have led to particle accumulation, increasing cluster sizes over time and potentially blocking the channels. This issue underscored the importance of hybrid nanofluids, as they offered a balanced composition

of multiple particle types, each with distinct advantages and limitations. However, while hybrid nanofluids offer enhanced heat transfer by leveraging the synergistic properties of different nanoparticles, they are not immune to these effects. In addition, the incorporation of metallic nanoparticles can pose risks of chemical reactivity, particularly when in contact with commonly used heat sink materials such as aluminium. This potential for corrosion or material degradation should be carefully considered in long-term applications.

To ensure the long-term viability of such systems, future work should investigate the rheological and chemical stability of nanofluids under

extended operating conditions. This includes conducting accelerated ageing tests, thermal cycling, and characterising particle dispersion using techniques such as dynamic light scattering and scanning electron microscopy. Consideration will also be given to surface treatments or protective coatings on channel materials to mitigate corrosion, as well as the use of environmentally friendly stabilisers or surfactant-free formulations that reduce degradation risks. These strategies are essential to transition nanofluid-enhanced cooling systems from laboratory-scale demonstrations to practical, scalable thermal management solutions in industrial settings.

Fig. 13 presented the average percentage enhancement of the Nusselt number compared to the base fluid (water) for both the IACPF and AICCPF configurations across different heating powers. The results demonstrated a clear trend where the enhancement in the Nusselt number decreased as heating power increased. At 75 W, the highest percentage enhancement was observed, particularly in the case of the Ag-SiC hybrid nanofluid, which exhibited a Nusselt number enhancement of 15.66% for IACPF and 17.56% for AICCPF. Among the simple nanofluids, Ag performed the best, with 13.37% and 15.31% enhancement in IACPF and AICCPF, respectively, followed by SiC (10.73% and 12.67%) and BeO (8.62% and 10.29%). The hybrid nanofluids consistently outperformed the simple nanofluids, with Ag-BeO reaching 13.38% and 16.45%, while SiC-BeO showed the lowest enhancement among hybrid formulations at 10.43% and 11.58%.

At 150 W, a slight decline was observed across all cases, with Ag-SiC still exhibiting the highest enhancement of 4.75% (IACPF) and 16.27% (AICCPF). Ag and SiC experienced moderate reductions of 13.04% and 14.6%, and 10.01% and 11.51%, respectively. BeO, which had the lowest thermal conductivity among the tested nanoparticles, showed the sharpest decline, dropping to 8.26% in IACPF and 8.75% in AICCPF. The hybrid nanofluids maintained their relative advantage, though the gap between them and simple nanofluids narrowed.

As the heating power increased to 225 W, the reduction in enhancement became more evident. The Ag-SiC hybrid nanofluid continued to outperform all other cases, maintaining 14.3% and 16% enhancement in IACPF and AICCPF, respectively. The simple nanofluids experienced further reductions, with Ag at 11.68% and 13.84%, SiC at

8.42% and 10.96%, and BeO at 7.31% and 7.88%. The decreasing trend indicated that while these nanofluids enhanced heat transfer, their relative efficiency declined as the heating load increased, possibly due to the effects of temperature-dependent thermal properties and increased particle interactions.

At the highest heating power of 300 W, the decline continued, with Ag-SiC maintaining its lead at 14.11% in IACPF and 15.68% in AICCPF. The Ag nanofluid, which initially exhibited strong performance, dropped to 10.59% and 13.41%, while SiC and BeO reached 7.91% and 10.19%, and 7.02% and 7.47%, respectively. The SiC-BeO hybrid nanofluid, which consistently showed lower enhancement, recorded the lowest values at 9.33% and 9.88%.

The results demonstrated that adopting a hybrid cooling approach, optimizing heat sink geometry, and utilizing coolants with superior thermal characteristics significantly enhanced heat transfer performance. This combined strategy effectively improved thermal regulation, making it a viable solution for high-power applications where efficient heat dissipation is critical.

6.4. Thermal resistance

The thermal resistance of a heat sink is a critical parameter that quantifies its ability to dissipate heat; lower thermal resistance indicates better heat dissipation performance. The thermal resistance of water, mono nanofluids, and hybrid nanofluids has been evaluated and discussed at a heating power of 300 W for IACPF and AICCPF. As anticipated, due to the maximum Nusselt number observed at this power, thermal resistance values are found to be the lowest for all fluids, as shown in Fig. 14.

Water exhibited the highest thermal resistance across all experimental cases. For the IACPF design, the thermal resistance of water decreased steadily from 0.02984 °C/W at a Reynolds number of approximately 130 to 0.02365 °C/W at a Reynolds number near 251. A similar declining trend was observed in the AICCPF configuration, with thermal resistance dropping from 0.02631 to 0.02086 °C/W. The AICCPF heat sink consistently demonstrated better thermal performance compared to the IACPF.

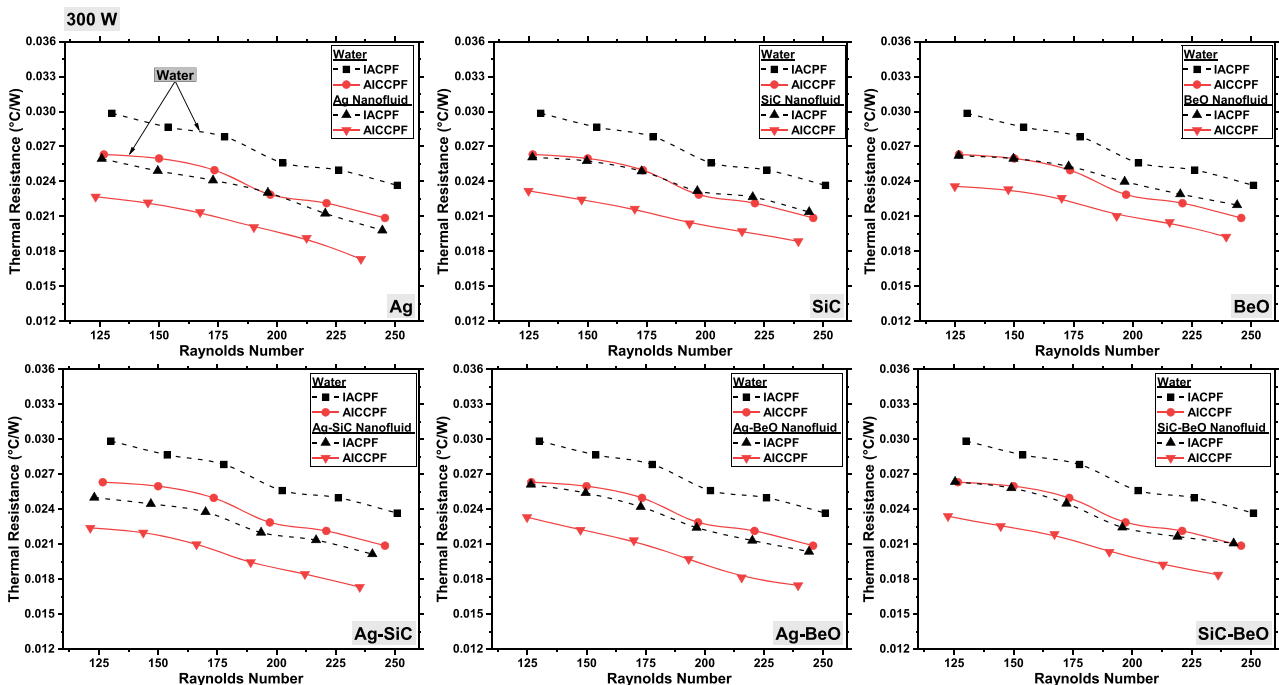


Fig. 14. Variation in thermal resistance against Reynolds number for IACPF and AICCPF configurations using various nanofluids at a constant heating power of 300 W.

When mono nanofluids were introduced, a noticeable improvement in thermal performance was observed. Silver nanofluid, owing to the exceptionally high thermal conductivity of nanoparticles, demonstrated significantly reduced thermal resistance in both configurations. In the IACPF arrangement, the resistance declined from 0.02595 to 0.0198 °C/W, whereas for AICCPF it ranged from 0.02269 to 0.01734 °C/W. This demonstrated the role of metallic nanoparticles in enhancing the convective heat transfer rate through improved thermal conduction pathways and nanoparticle–fluid interactions.

The SiC nanofluid also exhibited a reduction in thermal resistance compared to water, although their performance was slightly inferior to that of Ag nanofluids. For the IACPF system, the resistance decreased from 0.02606 to 0.02137 °C/W, while for the AICCPF counterpart, the values ranged from 0.02319 to 0.01886 °C/W. Beryllium oxide nanofluid behaved similarly, showing values between 0.02621 to 0.02197 °C/W in the IACPF design, and 0.02358 to 0.01925 °C/W in AICCPF. Though both BeO and SiC nanofluids demonstrated significant improvements over water, they were less effective than Ag nanofluids, due to their comparatively lower thermal conductivities.

The introduction of hybrid nanofluids led to even more promising outcomes. Ag/SiC nanofluids recorded thermal resistances as low as 0.02014 °C/W in IACPF and 0.01732 °C/W in AICCPF, making them one of the most effective fluids tested. The combined effects of Ag superior thermal conductivity and SiC thermal stability and wettability likely contributed to this synergistic enhancement. Similarly, Ag/BeO nanofluids also demonstrated notable reductions, reaching values of 0.02036 °C/W and 0.01746 °C/W in IACPF and AICCPF, respectively. Although both Ag-based hybrids showed comparable performance, Ag/SiC slightly outperformed Ag/BeO in the AICCPF setup, indicating favourable interaction and dispersion characteristics in that particular configuration. The SiC/BeO hybrid nanofluid, although slightly behind the SiC nanofluid, still showed marked improvement compared to water and mono BeO nanofluid. Its thermal resistance reduced to 0.02106 °C/W in IACPF and 0.01837 °C/W in AICCPF.

Fig. 15 presents the average percentage reduction in thermal resistance achieved by simple and hybrid nanofluids when applied to IACPF and AICCPF heat sinks. Among the simple nanofluids, Ag nanofluid demonstrated the most significant reduction in thermal resistance, achieving 17.55% for IACPF and 18.29% for AICCPF. In comparison, SiC and BeO nanofluids showed lower reductions, with SiC resulting in 13.28% and 13.8%, while BeO gave the smallest improvement, with reductions of 11.49% and 11.85% in IACPF and AICCPF, respectively.

The hybrid nanofluids displayed an even greater impact on thermal

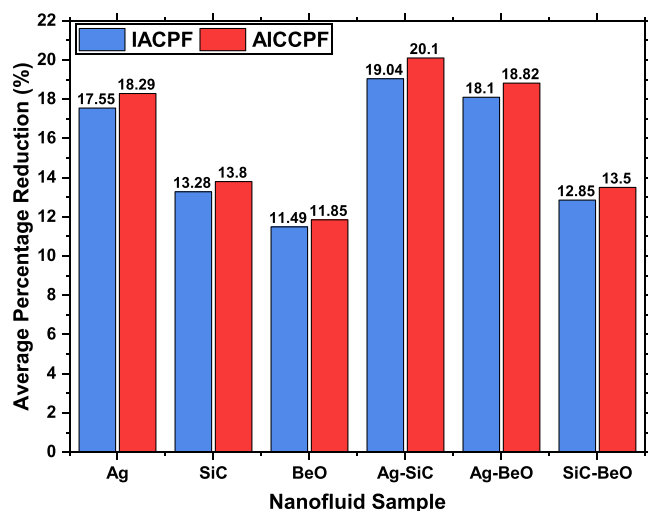


Fig. 15. Average percentage reduction in thermal resistance for simple and hybrid nanofluids in IACPF and AICCPF configurations at a constant heating power of 300 W.

resistance reduction. The Ag/SiC hybrid nanofluid emerged as the most efficient, with reductions of 19.04% for IACPF and 20.1% for AICCPF. Ag/BeO demonstrated a substantial reduction of 18.1% in IACPF and 18.82% in AICCPF, further supporting the role of silver as a dominant enhancer when used in combination with other particles. Finally, the SiC/BeO hybrid nanofluid resulted in a comparatively moderate reduction (12.85% and 13.5%). This indicates that while hybridization can improve thermal performance, the specific properties and interactions of the constituent nanoparticles play a critical role in determining overall effectiveness.

The results confirmed that nanofluids, especially hybrid ones, significantly reduced the thermal resistance of heat sinks under high thermal loads. Among the various fluids studied, Ag/SiC hybrid nanofluid demonstrated the most efficient thermal performance. Furthermore, the AICCPF design consistently outperformed the IACPF configuration across all fluid types, underlining the importance of geometrical optimization in thermal system design.

6.5. Wall temperature and logarithmic mean temperature difference

Wall temperature and Logarithmic Mean Temperature Difference (LMTD) are pivotal indicators for evaluating the thermal performance of cooling systems. The wall temperature specifically represents the temperature of the heat sink surface in direct contact with the working fluid and serves as a measure of the system's capacity to remove heat from the solid domain. A lower wall temperature is indicative of more effective heat transfer from the surface to the fluid. On the other hand, LMTD offers a broader view of the temperature driving potential across the heat sink, capturing the average thermal gradient between the solid surface and fluid along the flow path.

The comparative trends illustrated in Fig. 16(a) demonstrate a consistent reduction in wall temperature when Ag/SiC nanofluid was employed instead of water, across both IACPF and AICCPF configurations. In the IACPF setup, water-cooled surfaces exhibited wall temperatures ranging from 45.20 °C at the lowest Reynolds number down to 32.28 °C at the highest. When Ag/SiC nanofluid was used, the wall temperatures were systematically lower, dropping from 43.04 °C to 31.46 °C. The AICCPF configuration showed an even greater reduction, with water-cooled surfaces reaching a minimum of 31.67 °C, whereas the Ag/SiC nanofluid reduced it further to 30.18 °C. These reductions suggest that the presence of high-conductivity Ag and ceramic SiC nanoparticles enhanced the thermal conduction pathways at the fluid–solid interface, leading to more efficient heat removal.

In Fig. 16(b), the top right-hand chart illustrates the variation in LMTD with Reynolds number. The behaviour of the LMTD followed a consistent trend, showing a gradual decline with increasing Reynolds number. As anticipated, the Ag/SiC nanofluid consistently demonstrated lower LMTD values compared to water under equivalent flow conditions. In the AICCPF design, LMTD dropped from 8.16 °C with water to 6.83 °C with Ag/SiC at lower Reynolds numbers, and further down to 4.81 °C at the highest. These results suggest that the nanofluid was more effective in minimizing the temperature differential required to sustain heat transfer, thereby achieving closer thermal equilibrium between the fluid and surface.

To assess the internal thermal behaviour of the heat sinks, seven thermocouples were strategically embedded along the length to record the core temperature profiles. This spatial resolution allows for evaluating the longitudinal thermal gradient under varying flow rates and working fluids. Fig. 16(c,d) showed the axial temperature profiles for both the IACPF and AICCPF heat sinks using water and Ag/SiC nanofluid at flow rates ranging from 200 to 450 ml/min. It is important to note that the inlet fluid temperature was maintained close to 20 °C in all cases to ensure a consistent thermal condition across the experiments.

For both water and Ag/SiC nanofluid, the temperature consistently increased from the inlet to the outlet, as expected due to progressive heat accumulation along the flow direction. However, a distinct difference in

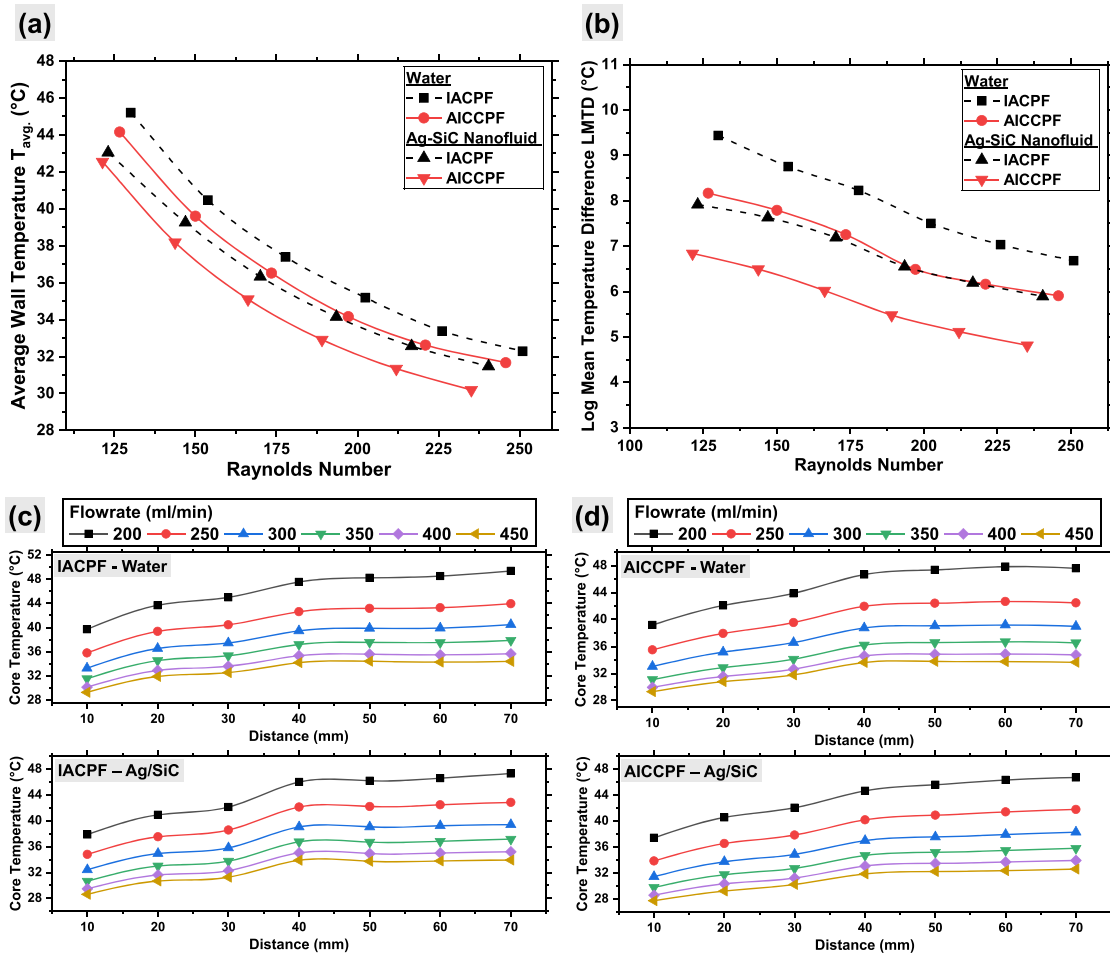


Fig. 16. Variation in (a) Average wall temperature, (b) Logarithmic Mean Temperature Difference (LMTD) across flow rates for Ag/SiC nanofluid compared to water, (c) Axial wall temperature distribution along the heat sink length.

the absolute temperature values and gradient steepness was observed between water and the nanofluid. At lower flow rates, the temperature rise along the heat sink length was steeper for water compared to Ag/SiC nanofluid, indicating inferior heat extraction capacity. As the flow rate increased, the temperature values at all locations along the length gradually decreased, reflecting enhanced convective cooling due to higher fluid velocity and reduced residence time within the channel.

In the IACPF configuration with water, wall temperatures increased progressively from approximately 39.7 °C at the 10 mm position to 49.4 °C at 70 mm when the flow rate was 200 ml/min. As the flow rate increased to 450 ml/min, this temperature range dropped significantly to 29.3 °C and 34.4 °C, respectively. A similar rising trend along the length was observed for all flow rates, although the gradient became less steep at higher flow rates due to enhanced convective cooling. When the Ag/SiC nanofluid was employed, the overall temperature values were notably reduced across all positions. At 200 ml/min, the temperature ranged from 37.9 °C to 47.3 °C, while at 450 ml/min, it further decreased to 28.6 °C and 33.9 °C. This reduction indicates improved heat transfer capability of the nanofluid, attributed to its superior thermal conductivity.

For the AICCPF configuration, the overall thermal performance was improved relative to IACPF, as reflected by the lower wall temperatures at corresponding positions and flow rates. With water, the wall temperature increased from around 39.2 °C to 47.6 °C at 200 ml/min and from 29.3 °C to 33.7 °C at 450 ml/min. The Ag/SiC nanofluid showed even better performance, with values spanning from 37.4 °C to 46.7 °C at 200 ml/min and from 27.7 °C to 32.6 °C at 450 ml/min.

Overall, a clear trend of decreasing wall temperature with increasing

flow rate is observed for all configurations, owing to the higher convective heat transfer. Additionally, the Ag/SiC nanofluid consistently outperformed water, and the AICCPF design demonstrated enhanced thermal regulation compared to IACPF, highlighting the combined benefits of advanced coolant and structural enhancement.

6.6. Pressure drop

Pressure drop is another critical parameter in the assessment of fluid flow and energy efficiency in thermal management systems. It arises due to frictional resistance and viscous dissipation as the fluid navigates through confined geometries. When nanofluids are employed to enhance heat transfer, their modified rheological properties can significantly impact the pressure drop characteristics. Therefore, understanding the interplay between flow rate (or Reynolds number) and pressure drop is essential to evaluating the trade-off between thermal performance and pumping power requirements.

The variation of pressure drop with Reynolds number has been investigated under different heating conditions, as shown in Fig. 17. In general, pressure drop increased with increasing Reynolds number across all fluid types and operating conditions. This is expected, as higher flow rates result in greater inertial effects and wall shear stresses, thereby increasing the frictional losses. Across all heating powers and fluid types, a consistent increasing trend of pressure drop with Reynolds number was observed. Additionally, it was observed that the AICCPF configuration consistently exhibited higher pressure drops than the IACPF configuration. This can be attributed to the presence of corrugated pin-fins in the AICCPF design, which increase flow resistance by

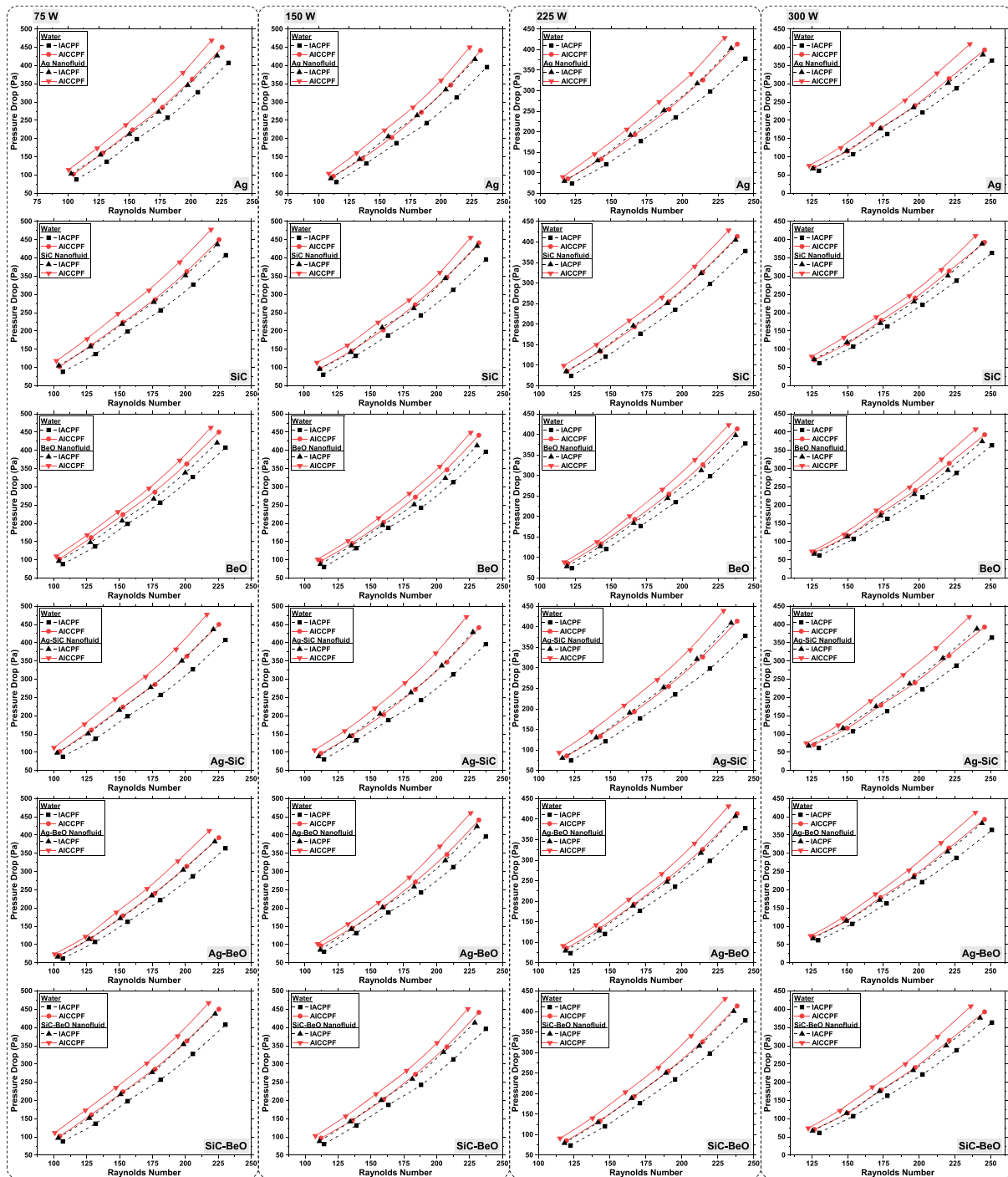


Fig. 17. Variation of pressure drop with Reynolds number for IACPF and AICCPF configurations under different heating powers using various nanofluids.

disrupting boundary layers and inducing local turbulence [76]. While this enhances heat transfer, it simultaneously intensifies pressure losses due to increased form drag and surface interactions.

Comparatively, nanofluids exhibit higher pressure drops than water, a result of increased viscosity and density caused by the suspended nanoparticles. Among the simple nanofluids, SiC nanofluid exhibited the highest pressure drop, reaching up to 478 Pa at $Re \approx 220$ under 75 W in the AICCPF configuration, which is approximately 15.86% higher than that of water at the same Reynolds number. This behaviour is attributed to the fact that silicon carbide nanoparticles possess sharp edges and irregular shapes, which disrupt the laminar flow more effectively than spherical particles, thereby increasing internal resistance and effective

viscosity [48]. The irregular morphology enhances fluid-particle interaction and momentum exchange, leading to a higher pressure penalty. In comparison, Ag and BeO nanofluids followed closely, with pressure drops of 469 Pa and 462 Pa, respectively.

Among the hybrid nanofluids investigated, the Ag/SiC nanofluid exhibited a pressure drop profile closely resembling that of the SiC nanofluid, despite having a higher proportion of Ag nanoparticles (mixing ratio: 0.6 Ag to 0.4 SiC). This trend suggests that the presence of SiC, with its irregular and angular morphology, exerts a dominant influence on the overall flow resistance, even when present in a lower fraction. The combined effect of metallic (Ag) and ceramic (SiC) nanoparticles likely contributes to increased fluid density and viscosity,

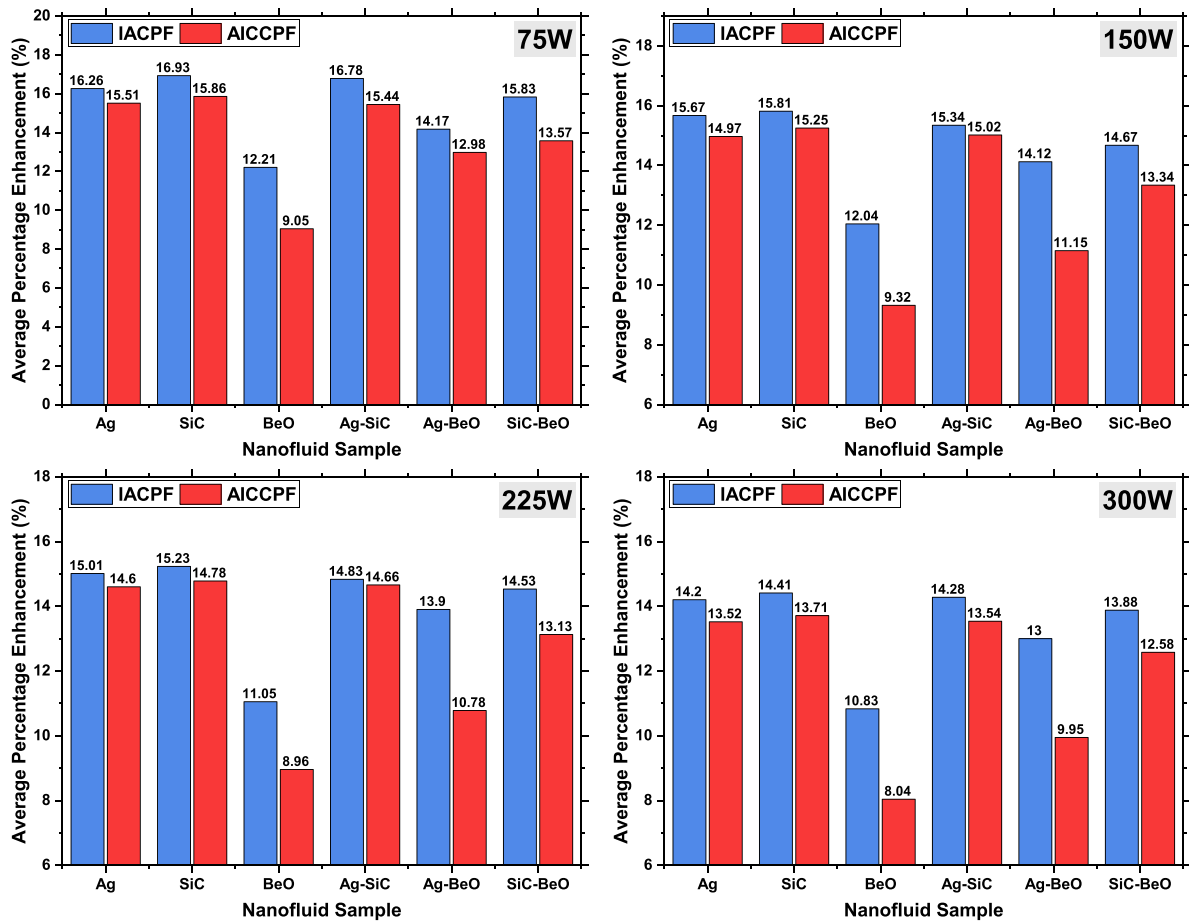


Fig. 18. Pressure drop enhancement of nanofluids relative to water across varying heating powers for IACPF and AICCPF configurations.

which in turn amplifies the pressure drop across the channels.

However, the Ag/BeO hybrid nanofluid exhibited a relatively lower pressure drop, with values generally falling between those observed for pure Ag and BeO nanofluids. This outcome is consistent with the particle characteristics: BeO nanoparticles are larger in size (85–140 nm), possess a hexagonal wurtzite structure, and exhibit random orientation, which may induce mild flow resistance. However, their smoother morphology compared to SiC still allows more streamlined flow, particularly when combined with the smaller and smoother Ag nanoparticles. Meanwhile, the SiC/BeO hybrid nanofluid displayed pressure drop values slightly below Ag/SiC but consistently higher than Ag/BeO, reflecting the intermediate effect of SiC’s irregular structure and BeO’s larger but less disruptive particles. This configuration results in moderately elevated viscosity and flow resistance compared to Ag/BeO, but slightly less than that of Ag/SiC. These observations underscore the critical role of nanoparticle morphology, density, crystal structure, and size distribution in influencing the hydrodynamic performance of hybrid nanofluids.

Fig. 18 shows the pressure drop enhancement of nanofluids relative to base fluid water across varying heating powers for both IACPF and AICCPF configurations. According to the results, a consistent decrease in pressure drop augmentation was observed with increasing thermal load, highlighting the temperature-dependent rheological behaviour of nanofluids.

At 75 W, the highest pressure drop enhancements were recorded across all nanofluids. In the IACPF configuration, SiC nanofluid exhibited the maximum enhancement of 16.93%, followed closely by the Ag/SiC and Ag hybrid nanofluids, with enhancements of 16.78% and 16.26%, respectively. BeO nanofluid showed the lowest enhancement of 12.21%. In the AICCPF system, values were slightly lower, 15.86% for

SiC, 15.51% for Ag, and 9.05% for BeO nanofluid.

At 150 W, a slight reduction in pressure drop was observed. SiC nanofluid showed an enhancement of 15.81% in IACPF and 15.25% in AICCPF. Ag nanofluid followed with 15.67% and 14.97% respectively, while BeO recorded 12.04% in IACPF and 9.32% in AICCPF. This downward trend continued at 225 W, where pressure drop enhancements decreased further. At the highest thermal load of 300 W, the pressure drop enhancements were the lowest. SiC and Ag nanofluids recorded 14.41% and 14.2% respectively in IACPF, and 13.71% and 13.52% in AICCPF. BeO further declined to 10.83% in IACPF and 8.04% in AICCPF.

Among the hybrid nanofluids, Ag/SiC consistently exhibited higher pressure drop values, closely following pure SiC. At 75 W, Ag/SiC showed an enhancement of 16.78% in IACPF and 15.44% in AICCPF, which gradually reduced to 14.28% and 13.54% respectively at 300 W. Ag/BeO presented the lowest pressure drop among the hybrids, starting at 14.17% in IACPF and 12.98% in AICCPF at 75 W, reducing to 13% and 9.95% at 300 W. SiC/BeO hybrid nanofluid displayed intermediate performance, with values decreasing from 15.83% to 13.88% in IACPF and from 13.57% to 12.58% in AICCPF.

These results confirm that increasing thermal power reduces the pressure drop enhancement due to lowered viscosity and improved flowability at higher temperatures. The hierarchy among the nanofluids remains consistent, with ceramic-based and hybrid nanofluids showing greater enhancements due to higher density and structural complexity.

The pressure drop study highlights not only the hydraulic performance of different nanofluids but also the broader influence of nanoparticle addition on fluid flow behaviour within mini-channel heat sinks. The introduction of nanoparticles increases the effective viscosity of the working fluid, thereby elevating flow resistance and contributing

to the observed rise in pressure losses compared to water. This effect was particularly evident with SiC and Ag/SiC nanofluids, which consistently exhibited the highest pressure drops due to their higher viscosity and stronger particle–fluid interactions.

Beyond viscosity, nanoparticle size, shape, and surface properties also affect flow characteristics. For instance, irregularly shaped particles like SiC can disrupt the local laminar profile, promoting enhanced micro-scale mixing while simultaneously increasing wall shear stress. In narrow channels, such effects are magnified due to the confined geometry, which makes particle–wall and particle–particle interactions more significant. Furthermore, regions of low flow velocity may experience temporary agglomeration or particle settling, leading to local constriction of flow pathways and non-uniform pressure distribution.

Despite the increase in hydraulic resistance, the presence of nanoparticles contributes positively to convective heat transfer by disturbing boundary layers and improving thermal conductivity. This presents a clear trade-off between enhanced thermal performance and increased pressure drop, which must be optimised based on the specific cooling requirements, allowable pumping power, and long-term operational stability of the system.

6.7. Performance improvement factor

The Performance Improvement Factor (PIF), also referred to as the thermal performance index (η), serves as a critical metric for evaluating the overall efficiency of a heat sink. It provides a balanced assessment by simultaneously considering enhancements in heat transfer and the associated rise in pressure drop or pumping power. Mathematically, the PIF is calculated as the ratio of the Nusselt number of the improved system to that of the base case, divided by the cube root of the corresponding friction factor ratio [77,78], represented with Eq. (25).

$$\text{Thermal Performance Index } (\eta) = \frac{Nu_{nc}/Nu_{bc}}{(f_{nc}/f_{bc})^{(1/3)}} \quad (25)$$

In the above equation, the term Nu_{nc} represents the Nusselt number corresponding to the new case, such as when a nanofluid is used or when the heat sink geometry is altered, for instance, in the AICCPF configuration. Nu_{bc} is the Nusselt number for the base case, typically calculated using water as the working fluid in the standard IACPF heat sink. Similarly, f_{nc} denotes the Darcy friction factor for the new case, accounting for the increased resistance to flow introduced by nanofluids or modified heat sink structures, whereas f_{bc} corresponds to the friction factor in the base case scenario.

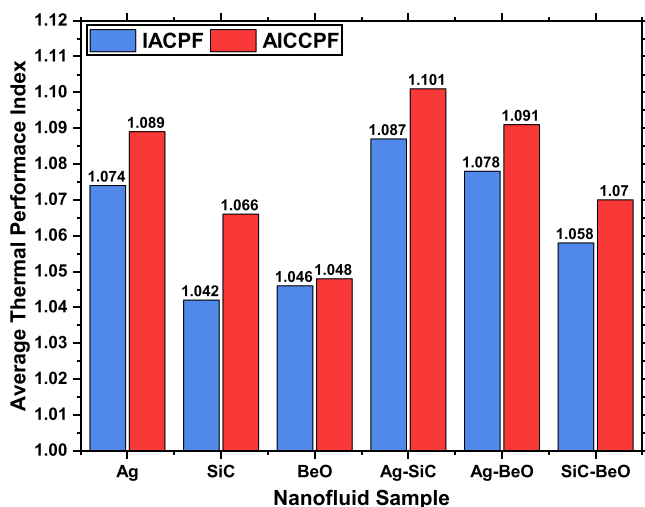


Fig. 19. Performance index comparison for all tested nanofluids in IACPF and AICCPF systems, showing optimal thermal-hydraulic efficiency of the AICCPF design.

This dimensionless index helps quantify how effectively a system can enhance heat transfer without disproportionately increasing flow resistance. In this study, the IACPF heat sink with water was considered as the baseline, while the AICCPF configuration was treated as the modified system. The comparative results between the two configurations are presented in Fig. 19. With water, the average thermal performance index of the AICCPF design was calculated to be 1.051, reflecting a moderate yet meaningful performance gain over the baseline.

When using nanofluids, all tested configurations demonstrated a PIF greater than unity, confirming that thermal performance improved relative to the water-cooled base case. Among the simple nanofluids, silver (Ag) nanofluid yielded the highest thermal performance index, with values of 1.074 for IACPF and 1.089 for AICCPF. This indicates a consistently superior heat transfer enhancement, even when accounting for the associated pressure drop.

The hybrid nanofluids showed further improvement. The Ag/SiC hybrid nanofluid delivered the best results, with a PIF of 1.087 for IACPF and 1.101 for AICCPF, making it the most thermally efficient fluid among all tested. Similarly, Ag/BeO and SiC/BeO hybrid nanofluids also outperformed their simple counterparts, with values of 1.078 and 1.058 for IACPF, and 1.091 and 1.070 for AICCPF, respectively.

Overall, the AICCPF system consistently showed higher performance indices than the IACPF, across all nanofluids tested. The enhancement confirms that the improved geometry, coupled with optimised nanofluid composition, delivers better heat transfer performance without an excessive increase in pumping power demand.

7. Concluding remarks, limitations, and future outlook

This study presented a comprehensive experimental investigation into the integration of nature-inspired heat sink geometries and nanofluid-based coolants to advance thermal management solutions for high-power-density applications. Two novel biomimetic configurations, IACPF and AICCPF, were tested under varying flow rates, thermal loads, and coolant compositions. The objective was to evaluate how nature-inspired geometries, combined with thermally optimised coolants, can enhance heat dissipation while maintaining acceptable hydraulic performance in mini/microchannel domains. The key findings of this study are summarised as follows:

1. The AICCPF configuration significantly outperformed the conventional straight-channel heat sink, achieving a 103% increase in Nusselt number with only a 37.5% rise in pressure drop at a heating power of 150 W. Additionally, it offered a 10.23% enhancement in Nusselt number over IACPF when using water at a lower thermal load of 75 W.
2. Among all tested scenarios, AICCPF heat sink with Ag/SiC hybrid nanofluid exhibited the most effective heat transfer performance. At the maximum thermal load of 300 W, it achieved an average Nusselt number enhancement of 17.56%, reaching up to 22.29% at the maximum flow rate, compared to water, outperforming all other working fluids and configurations evaluated in this study.
3. Thermal resistance showed notable variation depending on the fluid and configuration. All nanofluids outperformed water, with Ag nanofluid reducing resistance by 18.29%, while the Ag/SiC hybrid achieved a maximum reduction of 20.1% in the AICCPF design. However, in applications where cost constraints are more pressing, hybrid nanofluids like SiC/BeO still provided meaningful improvements, presenting a cost-effective alternative that balances thermal performance with affordability.
4. Pressure drop increased consistently with Reynolds number for all tested fluids, with nanofluids exhibiting higher values than water due to their elevated viscosity and intensified particle–fluid interactions. Among the mono nanofluids, SiC recorded the highest pressure drop in the AICCPF configuration, reaching 478 Pa, which represents a 15.86% increase compared to water. This was followed

- by Ag and BeO nanofluids, which produced pressure drops of 469 Pa and 462 Pa, respectively, under the same operating conditions.
- For hybrid nanofluids, Ag/SiC showed pressure drop behaviour similar to pure SiC, with an enhancement of up to 15.44% over water in AICCPF at 75 W, gradually decreasing to 13.54% at 300 W, reflecting the temperature-dependent reduction in fluid viscosity. However, Ag/BeO demonstrated the lowest pressure drop among the hybrid formulations, with enhancements reducing from 12.98% to 9.95% over the same thermal range. This relatively low hydraulic penalty makes Ag/BeO a favourable choice for systems where minimising pumping power and flow resistance is essential.
 - In terms of overall thermal-hydraulic efficiency, AICCPF combined with Ag/SiC hybrid nanofluid achieved the highest TPI of 1.101, indicating an optimal balance between heat transfer enhancement and pressure drop. All tested nanofluids delivered TPI values above unity, confirming the effectiveness of the proposed approach.

The results of this study demonstrate that combining bioinspired design with engineered nanofluids can significantly improve the cooling performance of compact systems without introducing excessive pressure losses. The corrugated airfoil-finned biomimetic geometry, in particular, enables superior fluid mixing and surface interaction, which is further amplified by the enhanced thermal conductivity of hybrid nanofluids.

While this study primarily focused on the short-term thermal and hydraulic evaluation of biomimetic heat sink configurations using mono and hybrid nanofluids, it is recognised that long-term performance and reliability are critical for real-world deployment. Future research will therefore aim to assess the stability of nanofluids under extended operational conditions, including thermal cycling and continuous flow, to understand the effects of agglomeration, sedimentation, and surface fouling over time. These efforts will involve accelerated ageing tests, monitoring of thermophysical property variations, and in-depth surface analysis using SEM, EDX, and FTIR to investigate nanoparticle interaction with channel surfaces and potential corrosion effects, particularly in aluminium-based systems. Furthermore, alternative nanofluid formulations, including environmentally friendly dispersants and surfactant-free systems, will be explored to improve chemical durability and sustainability. There is also scope to investigate active control strategies, such as pulsed flow or periodic flow reversal, to enhance redistribution of particles and maintain heat transfer efficiency in mini- and micro-channel domains. These research directions aim to transform the promising short-term performance demonstrated in this study into robust, scalable, and low-maintenance thermal management solutions for industrial applications.

Looking ahead, the biomimetic heat sink designs developed in this study hold vast potential beyond conventional thermal management. While their immediate impact lies in enhancing cooling efficiency in applications such as electric vehicles, data centres, and compact electronics, the underlying design philosophy inspired by aquatic respiration systems offers opportunities far beyond heat dissipation. The proposed configurations demonstrated here can be adapted for use in emerging technologies such as drones, flying cars, and urban air mobility platforms where fluid flow optimization, structural lightness, and multifunctionality are crucial. These geometries not only support effective thermal control but can also be reimagined as aerodynamic components, propulsion housings, or integrated passive ventilation systems. Thus, the nature-inspired approach showcased in this work establishes a design framework that merges thermal functionality with aerodynamic efficiency, paving the way for innovative, multifunctional systems in the future of mobility, aerospace, and smart device engineering.

CRedit authorship contribution statement

Hamza Babar: Writing – original draft, Visualization, Validation, Methodology, Investigation, Formal analysis, Data curation,

Conceptualization, Software. **Hongwei Wu:** Writing – review & editing, Supervision, Funding acquisition, Resources. **Mahmoud Eltaweel:** Writing – review & editing, Validation, Visualization. **Wenbin Zhang:** Writing – review & editing, Supervision.

Declaration of competing interest

The authors declare that they have no known competing financial interests or personal relationships that could have appeared to influence the work reported in this paper.

Acknowledgement

The authors gratefully acknowledge the financial support provided by the Royal Society through the International Exchanges Scheme (Grant No. IES\R3\223052) and the Engineering and Physical Sciences Research Council (EPSRC), United Kingdom (Grant No. EP/X038319/1), under the framework of the Horizon Europe Marie Skłodowska-Curie Actions (MSCA) project (Grant No. 101082394).

Data availability

Data will be made available on request.

References

- The Data Center Liquid Cooling Technology Transition: Benchmarking the Market, (2025). <https://www.datacenterfrontier.com/white-papers/whitepaper/55260442/the-data-center-liquid-cooling-technology-transition-benchmarking-the-market>.
- Uptime Institute's Global Data Center Survey Results 2023, (2023). <https://uptimeinstitute.com/resources/research-and-reports/uptime-institute-global-data-center-survey-results-2023>.
- S.M. Sohel Murshed, C.A. Nieto de Castro, A critical review of traditional and emerging techniques and fluids for electronics cooling, *Renew. Sustain. Energy Rev.* 78 (2017) 821–833, <https://doi.org/10.1016/j.rser.2017.04.112>.
- H. Babar, H. Wu, W. Zhang, T.R. Shah, D. McCluskey, C. Zhou, The promise of nanofluids: a bibliometric journey through advanced heat transfer fluids in heat exchanger tubes, *Adv. Colloid Interface Sci.* 325 (2024) 103112, <https://doi.org/10.1016/j.cis.2024.103112>.
- M. Muneeshwaran, G. Srinivasan, P. Muthukumar, C.C. Wang, Role of hybrid-nanofluid in heat transfer enhancement—a review, *Int. Commun. Heat Mass Transf.* 125 (2021) 105341, <https://doi.org/10.1016/j.icheatmasstransfer.2021.105341>.
- T.R. Shah, H.M. Ali, Applications of hybrid nanofluids in solar energy, practical limitations and challenges: a critical review, *Sol. Energy* 183 (2019) 173–203, <https://doi.org/10.1016/j.solener.2019.03.012>.
- H.A. Hasan, H. Togun, A.M. Abed, N.A.A. Qasem, H.I. Mohammed, A. Abderrahmane, K. Guedri, E.S.M. Tag-ElDin, Efficient cooling system for lithium-ion battery cells by using different concentrations of nanoparticles of SiO₂-water: a numerical investigation, *Symmetry* 15 (2023) 640, <https://doi.org/10.3390/sym15030640>.
- F.A. Abood, S.J. Yaseen, I.G. Mohammed, R.Z. Homod, H.I. Mohammed, Enhancing thermal performance in a magnetized square cavity: novel insights from mixed convection of Ag-MgO nanofluid around a rotating cylinder, *Int. J. Thermofluids* 22 (2024) 100630, <https://doi.org/10.1016/j.ijft.2024.100630>.
- R. Ellahi, A. Zeeshan, N. Shehzad, S.Z. Alamri, Structural impact of kerosene-Al₂O₃ nanoliquid on MHD Poiseuille flow with variable thermal conductivity: application of cooling process, *J. Mol. Liq.* 264 (2018) 607–615, <https://doi.org/10.1016/j.molliq.2018.05.103>.
- Q. Zhang, Z. Feng, J. Zhang, F. Guo, S. Huang, Z. Li, Design of a mini-channel heat sink for high-heat-flux electronic devices, *Appl. Therm. Eng.* 216 (2022) 119053, <https://doi.org/10.1016/j.applthermaleng.2022.119053>.
- T. Dixit, I. Ghosh, Review of micro- and mini-channel heat sinks and heat exchangers for single phase fluids, *Renew. Sustain. Energy Rev.* 41 (2015) 1298–1311, <https://doi.org/10.1016/j.rser.2014.09.024>.
- R. Ellahi, A. Zeeshan, S. Shafique, S.M. Sait, A. Ur Rehman, Electroosmotic slip flow in peristaltic transport of non-newtonian third-grade MHD fluid: RSM-based sensitivity analysis, *Int. J. Heat Mass Transf.* 247 (2025) 127121, <https://doi.org/10.1016/j.ijheatmasstransfer.2025.127121>.
- Y.T. Li, S. Zhao, K. Zhang, G. Lu, Y. Li, Extremely high heat flux dissipation and hotspots removal with nature-inspired single-phase microchannel heat sink designs, *Appl. Therm. Eng.* 234 (2023) 121282, <https://doi.org/10.1016/j.applthermaleng.2023.121282>.
- S. Acharya, Thermo-fluidic analysis of microchannel heat sink with inline/staggered square/elliptical fins, *Int. Commun. Heat Mass Transf.* 147 (2023) 106961, <https://doi.org/10.1016/j.icheatmasstransfer.2023.106961>.
- J. Mehboob, R. Ellahi, S.M. Sait, N.S. Akbar, Optimizing bioconvective heat transfer with MHD Eyring–Powell nanofluids containing motile microorganisms with viscosity variability and porous media in ciliated microchannels, *Int. J.*

- Numer. Methods Heat Fluid Flow 35 (2025) 825–846, <https://doi.org/10.1108/HFF-11-2024-0838>.
- [16] Y. Wang, X. Xu, Z. Liu, J. Kong, Q. Zhai, H. Zakaria, Q. Wang, F. Zhou, H. Wei, Optimization of liquid cooling for prismatic battery with novel cold plate based on butterfly-shaped channel, *J. Energy Storage* 73 (2023) 109161, <https://doi.org/10.1016/j.est.2023.109161>.
- [17] A. Alkhazaleh, F. Alnaimat, B. Mathew, Characterization of MEMS heat sinks having straight microchannels integrating square pin-fins for liquid cooling of microelectronic chips, *Therm. Sci. Eng. Prog.* 45 (2023) 102154, <https://doi.org/10.1016/j.tsep.2023.102154>.
- [18] H.K. Pazarlıoğlu, E. Gürsoy, M. Gürdal, Z. Said, K. Arslan, E. Gedik, Numerical simulation of sudden expansion tubes with Ag-MgO nanofluid and innovative fin structure: a thermo-fluidic analysis, *Int. J. Heat Fluid Flow* 108 (2024), <https://doi.org/10.1016/j.ijheatfluidflow.2024.109448>.
- [19] W. Duangthongsuk, S. Laohalertdecha, S. Wongwises, Experimental study on the thermo-thermal performance of nanofluids-cooled heat sinks with diamond shape micro pin-fin structures, *Int. J. Thermofluids* 22 (2024) 100691, <https://doi.org/10.1016/j.ijft.2024.100691>.
- [20] W. Gao, J. Meng, Z. Qu, J. Zhang, Experimental and numerical study on thermofluidic characteristics of microchannel heat sinks with various micro pin-fin arrays arrangement patterns, *Appl. Therm. Eng.* 240 (2024) 122236, <https://doi.org/10.1016/j.applthermaleng.2023.122236>.
- [21] S. Gijoy, M.A. Gayathri, S. Rejin, K.E.R. Roy, Numerical investigation and optimization of an asymmetric elliptical-cylindrical pin fin heat sink, *Int. J. Therm. Sci.* 209 (2025) 109514, <https://doi.org/10.1016/j.ijthermalsci.2024.109514>.
- [22] H. Babar, H.M. Ali, Airfoil shaped pin-fin heat sink: potential evaluation of ferric oxide and titania nanofluids, *Energy Convers. Manag.* 202 (2019) 112194, <https://doi.org/10.1016/j.enconman.2019.112194>.
- [23] H.K. Pazarlıoğlu, Parametric analyses of finned heatsink filled with Fe₃O₄/water regarding thermodynamic irreversibility, *Düzce Üniv. Tek. Bilim. Der. 1* (2023) 1–10. <https://dergipark.org.tr/en/pub/duted/issue/81799/1366695>.
- [24] M. Bahraei, N. Mazaheri, M.R. Daneshyar, Employing elliptical pin-fins and nanofluid within a heat sink for cooling of electronic chips regarding energy efficiency perspective, *Appl. Therm. Eng.* 183 (2021) 116159, <https://doi.org/10.1016/j.applthermaleng.2020.116159>.
- [25] R. Ellahi, The effects of MHD and temperature dependent viscosity on the flow of non-newtonian nanofluid in a pipe: analytical solutions, *Appl. Math. Model.* 37 (2013) 1451–1467, <https://doi.org/10.1016/j.apm.2012.04.004>.
- [26] F. Han, H. Guo, X. Ding, Design and optimization of a liquid cooled heat sink for a motor inverter in electric vehicles, *Appl. Energy* 291 (2021) 116819, <https://doi.org/10.1016/j.apenergy.2021.116819>.
- [27] H.E. Ahmed, B.H. Salman, A.S. Kherbeet, M.I. Ahmed, Optimization of thermal design of heat sinks: a review, *Int. J. Heat Mass Transf.* 118 (2018) 129–153, <https://doi.org/10.1016/j.ijheatmasstransfer.2017.10.099>.
- [28] Y. Li, S. Roux, C. Castelain, Y. Fan, L. Luo, Design and optimization of heat sinks for the liquid cooling of electronics with multiple heat sources: a literature review, *Energies* 16 (2023) 7468, <https://doi.org/10.3390/en16227468>.
- [29] S. Ki, J. Lee, S. Ryu, S. Bang, K. Kim, Y. Nam, A bio-inspired, low pressure drop liquid cooling system for high-power IGBT modules for EV/HEV applications, *Int. J. Therm. Sci.* 161 (2021) 106708, <https://doi.org/10.1016/j.ijthermalsci.2020.106708>.
- [30] W. Song, W. Lu, S. Yu, R. Tang, X. Xie, X. Zhou, Z. Chen, Evaluating a novel portable semiconductor liquid cooling garment for reducing heat stress of healthcare workers in a hot-humid environment, *Build. Environ.* 267 (2025) 112194, <https://doi.org/10.1016/j.buildenv.2024.112194>.
- [31] G.C. Birur, T.W. Sur, A.D. Paris, P. Shakkottai, A.A. Green, S.I. Haapanen, Micro/nano spacecraft thermal control using a MEMS-based pumped liquid cooling system, in: C.H. Mastrangelo, H. Becker (Eds.), 2001: pp. 196–206. [10.1117/1.2.443059](https://doi.org/10.1117/1.2.443059).
- [32] C. Zhao, M. Clarke, H. Kellermann, D. Verstraete, Liquid cooling systems for batteries of electric vertical takeoff and landing aircraft, *J. Aircr.* 61 (2024) 667–683, <https://doi.org/10.2514/1.C037404>.
- [33] S.S. Ghadikolaei, S. Siahchehrehghadikolaei, M. Gholinia, M. Rahimi, A CFD modeling of heat transfer between CGNPs/H₂O eco-friendly nanofluid and the novel nature-based designs heat sink: hybrid passive techniques for CPU cooling, *Therm. Sci. Eng. Prog.* 37 (2023) 101604, <https://doi.org/10.1016/j.tsep.2022.101604>.
- [34] A. Shahsavari, M. Hasani, A. Alizadeh, Two-phase simulation of hydrothermal performance and entropy generation aspects of a biologically prepared nanofluid-cooled heat sink with helical Tesla valve-based microchannels, *Case Stud. Therm. Eng.* 58 (2024) 104429, <https://doi.org/10.1016/j.csite.2024.104429>.
- [35] D. Kong, H. Kwon, B. Jang, H.J. Kwon, M. Asheghi, K.E. Goodson, H. Lee, Extreme heat flux cooling from functional copper inverse opal-coated manifold microchannels, *Energy Convers. Manag.* 315 (2024) 118809, <https://doi.org/10.1016/j.enconman.2024.118809>.
- [36] F. Zhang, Z. Huang, S. Li, S. Sun, H. Zhao, Design and thermal performance analysis of a new micro-fin liquid cooling plate based on liquid cooling channel finning and bionic limulus-like fins, *Appl. Therm. Eng.* 237 (2024) 121597, <https://doi.org/10.1016/j.applthermaleng.2023.121597>.
- [37] S. Gupta, P.M.V. Subbarao, Empirical investigation of nanofluid performance in a microchannel heat sink for various attributes in low Reynolds number range, *Int. J. Heat Fluid Flow* 105 (2024) 109258, <https://doi.org/10.1016/j.ijheatfluidflow.2023.109258>.
- [38] Z. Ma, C. Hu, L. Ma, H. Chen, J. Hou, N. Hao, J. Wei, Nanofluids in microchannel heat sinks for efficient flow cooling of power electronic devices, *Appl. Mater. Today* 35 (2023) 101980, <https://doi.org/10.1016/j.apmt.2023.101980>.
- [39] N. Zhao, L. Guo, C. Qi, T. Chen, X. Cui, Experimental study on thermo-hydraulic performance of nanofluids in CPU heat sink with rectangular grooves and cylindrical bugles based on exergy efficiency, *Energy Convers. Manag.* 181 (2019) 235–246, <https://doi.org/10.1016/j.enconman.2018.11.076>.
- [40] J. Sun, W. Wang, J. Zhang, R. Zhang, J. Li, Study on heat transfer characteristics of matrix rib micro-jet heat sink based on SiC nanofluids, *Int. J. Therm. Sci.* 194 (2023) 108591, <https://doi.org/10.1016/j.ijthermalsci.2023.108591>.
- [41] J. Wang, S. Qi, Z. Xu, Y. Xu, Experimental investigation of the thermal-hydraulic characteristics of liquid cooling heat sinks with novel pin fins, *Case Stud. Therm. Eng.* 55 (2024) 104172, <https://doi.org/10.1016/j.csite.2024.104172>.
- [42] C. Qi, J. Hu, M. Liu, L. Guo, Z. Rao, Experimental study on thermo-hydraulic performances of CPU cooled by nanofluids, *Energy Convers. Manag.* 153 (2017) 557–565, <https://doi.org/10.1016/j.enconman.2017.10.041>.
- [43] N.L.N. Yusof, H.S. Shamsuddin, P. Estellé, N. Mohd-Ghazali, Optimization of a boron nitride nanotubes nanofluid-cooled microchannel heat sink at different concentrations, *J. Therm. Anal. Calorim.* 148 (2023) 3117–3127, <https://doi.org/10.1007/s10973-022-11545-8>.
- [44] T. Baig, A. Adil, S. Manzoor, M. Ebrahem, H.A. Tariq, H.M. Ali, Thermal performance of dual flow slotted fin mini channel heat sink using Al₂O₃-H₂O and TiO₂-H₂O: a numerical and experimental approach, *Nanotechnology* 34 (2023) 425405, <https://doi.org/10.1088/1361-6528/ace82f>.
- [45] S.E. Ghasemi, A.A. Ranjbar, M.J. Hoseini, S. Mohsenian, Design optimization and experimental investigation of CPU heat sink cooled by alumina-water nanofluid, *J. Mater. Res. Technol.* 15 (2021) 2276–2286, <https://doi.org/10.1016/j.jmrt.2021.09.021>.
- [46] E.D. Stevens, Some aspects of gas exchange in Tuna, *J. Exp. Biol.* 56 (1972) 809–823, <https://doi.org/10.1242/jeb.56.3.809>.
- [47] P. Zhang, T. Cui, Q. Li, Effect of surface roughness on thermal contact resistance of aluminium alloy, *Appl. Therm. Eng.* 121 (2017) 992–998, <https://doi.org/10.1016/j.applthermaleng.2017.04.142>.
- [48] H. Babar, H. Wu, W. Zhang, Y. Xie, Harnessing nano-synergy: a comprehensive study of thermophysical characteristics of silver, beryllium oxide, and silicon carbide in hybrid nanofluid formulations, *J. Mol. Liq.* 414 (2024) 126175, <https://doi.org/10.1016/j.molliq.2024.126175>.
- [49] Y. Xuan, W. Roetzel, Conceptions for heat transfer correlation of nanofluids, *Int. J. Heat Mass Transf.* 43 (2000) 3701–3707, [https://doi.org/10.1016/S0017-9310\(99\)00369-5](https://doi.org/10.1016/S0017-9310(99)00369-5).
- [50] B. Bhattacharjee, S. Dutta, T. Maity, S. Dey, S. Mondal, S. Bhowmick, Impacts of nanofluids and nanomaterials on environment and human health: a review, *Nanosci. Nanotechnol. Asia* 13 (2023), <https://doi.org/10.2174/2210681213666230601103342>.
- [51] M.J. Lourenço, J. Alexandre, C. Huisman, X. Paredes, C. Nieto de Castro, The balance between energy, environmental security, and technical performance: the regulatory challenge of nanofluids, *Nanomaterials* 11 (2021) 1871, <https://doi.org/10.3390/nano11081871>.
- [52] Z. Said, L.S. Sundar, A.K. Tiwari, H.M. Ali, M. Sheikholeslami, E. Bellos, H. Babar, Recent advances on the fundamental physical phenomena behind stability, dynamic motion, thermophysical properties, heat transport, applications, and challenges of nanofluids, *Phys. Rep.* 946 (2022) 1–94, <https://doi.org/10.1016/j.physrep.2021.07.002>.
- [53] H. Babar, H. Wu, H.M. Ali, T.R. Shah, W. Zhang, Staggered oriented airfoil shaped pin-fin heat sink: investigating the efficacy of novel water based ferric oxide-silica hybrid nanofluid, *Int. J. Heat Mass Transf.* 194 (2022) 123085, <https://doi.org/10.1016/j.ijheatmasstransfer.2022.123085>.
- [54] N.N. Esfahani, D. Toghraie, M. Afrand, A new correlation for predicting the thermal conductivity of ZnO–Ag (50%–50%)/water hybrid nanofluid: an experimental study, *Powder Technol.* 323 (2018) 367–373, <https://doi.org/10.1016/j.powtec.2017.10.025>.
- [55] F. Chen, L. Zhang, X. Huai, J. Li, H. Zhang, Z. Liu, Comprehensive performance comparison of airfoil fin PCHes with NACA 00XX series airfoil, *Nucl. Eng. Des.* 315 (2017) 42–50, <https://doi.org/10.1016/j.nucengdes.2017.02.014>.
- [56] X. Cui, J. Guo, X. Huai, K. Cheng, H. Zhang, M. Xiang, Numerical study on novel airfoil fins for printed circuit heat exchanger using supercritical CO₂, *Int. J. Heat Mass Transf.* 121 (2018) 354–366, <https://doi.org/10.1016/j.ijheatmasstransfer.2018.01.015>.
- [57] P. Naphon, L. Nakharintr, Heat transfer of nanofluids in the mini-rectangular fin heat sinks, *Int. Commun. Heat Mass Transf.* 40 (2013) 25–31, <https://doi.org/10.1016/j.icheatmasstransfer.2012.10.012>.
- [58] N.A. Roberts, D.G. Walker, Convective performance of nanofluids in commercial electronics cooling systems, *Appl. Therm. Eng.* 30 (2010) 2499–2504, <https://doi.org/10.1016/j.applthermaleng.2010.06.023>.
- [59] C.J. Ho, Y.N. Chung, C.M. Lai, Thermal performance of Al₂O₃/water nanofluid in a natural circulation loop with a mini-channel heat sink and heat source, *Energy Convers. Manag.* 87 (2014) 848–858, <https://doi.org/10.1016/j.enconman.2014.07.079>.
- [60] H.K. Pazarlıoğlu, A.Ü. Tepe, K. Arslan, Thermohydraulic performance assessment of new alternative methods for anti-icing application against current application in an aircraft, *Proc. Inst. Mech. Eng. Part E J. Process Mech. Eng.* 239 (2025) 1477–1493, <https://doi.org/10.1177/09544089231190182>.
- [61] M.R. Sohel, S.S. Khaleduzzaman, R. Saidur, A. Hepbasli, M.F.M. Sabri, I. M. Mahbubul, An experimental investigation of heat transfer enhancement of a minichannel heat sink using Al₂O₃-H₂O nanofluid, *Int. J. Heat Mass Transf.* 74 (2014) 164–172, <https://doi.org/10.1016/j.ijheatmasstransfer.2014.03.010>.
- [62] R.K. Shah, Thermal entry length solutions for the circular tube and parallel plates, in: *Proceedings of 3rd National Heat and Mass Transfer Conference, Indian Institute of Technology Bombay Delhi, 1975*, pp. 11–75.

- [63] A. Qamar, R. Shaukat, S. Imran, M. Farooq, M. Amjad, Z. Anwar, H. Ali, M. Farhan, M.A. Mujtaba, T. Korakianitis, M.A. Kalam, F. Almomani, Effect of surfactants on the convective heat transfer and pressure drop characteristics of ZnO/DIW nanofluids: an experimental study, *Case Stud. Therm. Eng.* 42 (2023) 102716, <https://doi.org/10.1016/j.csite.2023.102716>.
- [64] Z. Wan, W. Quan, C. Yang, H. Yan, X. Chen, T. Huang, X. Wang, S. Chan, Optimal design of a novel M-like channel in bipolar plates of proton exchange membrane fuel cell based on minimum entropy generation, *Energy Convers. Manag.* 205 (2020) 112386, <https://doi.org/10.1016/j.enconman.2019.112386>.
- [65] Y. He, Y. Jin, H. Chen, Y. Ding, D. Cang, H. Lu, Heat transfer and flow behaviour of aqueous suspensions of TiO₂ nanoparticles (nanofluids) flowing upward through a vertical pipe, *Int. J. Heat Mass Transf.* 50 (2007) 2272–2281, <https://doi.org/10.1016/j.ijheatmasstransfer.2006.10.024>.
- [66] E.B. Haghghi, M. Saleemi, N. Nikkam, R. Khodabandeh, M.S. Toprak, M. Muhammed, B. Palm, Accurate basis of comparison for convective heat transfer in nanofluids, *Int. Commun. Heat Mass Transf.* 52 (2014) 1–7, <https://doi.org/10.1016/j.icheatmasstransfer.2014.01.002>.
- [67] M. Liu, D. Liu, S. Xu, Y. Chen, Experimental study on liquid flow and heat transfer in micro square pin fin heat sink, *Int. J. Heat Mass Transf.* 54 (2011) 5602–5611, <https://doi.org/10.1016/j.ijheatmasstransfer.2011.07.013>.
- [68] H. Babar, H. Wu, W. Zhang, Investigating the performance of conventional and hydrophobic surface heat sink in managing thermal challenges of high heat generating components, *Int. J. Heat Mass Transf.* 216 (2023) 124604, <https://doi.org/10.1016/j.ijheatmasstransfer.2023.124604>.
- [69] K.P. Griffin, L. Fu, P. Moin, General method for determining the boundary layer thickness in nonequilibrium flows, *Phys. Rev. Fluids* 6 (2021) 024608, <https://doi.org/10.1103/PhysRevFluids.6.024608>.
- [70] E. Tavousi, N. Perera, D. Flynn, R. Hasan, Heat transfer and fluid flow characteristics of the passive method in double tube heat exchangers: a critical review, *Int. J. Thermofluids* 17 (2023) 100282, <https://doi.org/10.1016/j.ijft.2023.100282>.
- [71] M.A. Al-Obaidi, F.L. Rashid, M.K. Rasheed, H.S.S. Aljibori, H.I. Mohammed, A. J. Mahdi, S. Ahmad, K. Al-Farhany, I.M. Mujtaba, Recent achievements in heat transfer enhancement with hybrid nanofluid in heat exchangers: a comprehensive review, *Int. J. Thermophys.* 45 (2024) 133, <https://doi.org/10.1007/s10765-024-03428-x>.
- [72] H. Babar, H.M. Ali, Towards hybrid nanofluids: preparation, thermophysical properties, applications, and challenges, *J. Mol. Liq.* 281 (2019) 598–633, <https://doi.org/10.1016/j.molliq.2019.02.102>.
- [73] M.Z. Saghir, M.M. Rahman, Brownian motion and thermophoretic effects of flow in channels using nanofluid: a two-phase model, *Int. J. Thermofluids* 10 (2021) 100085, <https://doi.org/10.1016/j.ijft.2021.100085>.
- [74] F.L. Rashid, H.S. Aljibori, H.I. Mohammed, A. Ameen, S. Ahmad, M.B. Ben Hamida, A.H. Al-Rubaye, Recent advances and developments of the application of hybrid nanofluids in parabolic solar collector energy systems and guidelines for future prospects, *J. Eng. Res.* (2024), <https://doi.org/10.1016/j.jer.2024.04.023>.
- [75] M. Zargartalebi, J. Azaiez, Heat transfer analysis of nanofluid based microchannel heat sink, *Int. J. Heat Mass Transf.* 127 (2018) 1233–1242, <https://doi.org/10.1016/j.ijheatmasstransfer.2018.07.152>.
- [76] M. Khoshvagt-Aliabadi, F. Nozan, Water cooled corrugated minichannel heat sink for electronic devices: effect of corrugation shape, *Int. Commun. Heat Mass Transf.* 76 (2016) 188–196, <https://doi.org/10.1016/j.icheatmasstransfer.2016.05.021>.
- [77] M. Harris, H. Babar, H. Wu, Assessing thermohydraulic performance in novel micro pin-fin heat sinks: a synergistic experimental, agile manufacturing, and machine learning approach, *Int. J. Heat Mass Transf.* 239 (2025) 126581, <https://doi.org/10.1016/j.ijheatmasstransfer.2024.126581>.
- [78] Y. Xu, L. Li, J. Wang, Experimental and numerical investigations of the thermal-hydraulic characteristics of novel micropin-fin heat sinks, *Int. J. Heat Mass Transf.* 209 (2023) 124079, <https://doi.org/10.1016/j.ijheatmasstransfer.2023.124079>.